Rocket Observation of sub-relativistic electrons in the quiet dayside auroral ionosphere

T. Namekawa[1,2], T. Mitani[1], K. Asamura[1], Y. Miyoshi[3], K. Hosokawa[4], Y. Ogawa[5], S. Saito[6], T. Hori[3], S. Sugo[2], O. Kawashima[2], S. Kasahara[2], R. Nomura[1], N. Yagi[7], M. Fukizawa[7], T. Sakanoi[7], Y. Saito[1], A. Matsuoka[8], I. Shinohara[1], Y. Fedorenko[9], A. Nikitenko[9], C. Koehler[10,11]

[1]Japan Aerospace Exploration Agency, Japan, [2]The University of Tokyo, Japan, [3]Nagoya University, Japan, [4]The University of Electro-Communications, Japan, [5]National Institute of Polar Research, Japan, [6]National Institute of Information and Communications Technology, Japan, [7]Tohoku University, Japan, [8]Kyoto University, Japan, [9]Polar Geophysical Institute, Russia, [10]Colorado Space Grant Consortium, USA, [11]University of Colorado at Boulder, USA

Corresponding author: Taku Namekawa (namekawa@stp.isas.jaxa.jp)

Key Points:

- A sounding rocket observed an energy spectrum of sub-relativistic electron precipitation in the dayside polar ionosphere for the first time.
- Ground-based and satellite observations and simulation show that the observed electron precipitation was caused by chorus waves.
- From the relation between the chorus wave and the aurora, the observed electrons likely to coincide with dayside pulsating/diffuse aurora.

Abstract

An energy spectrum of electrons from 180 keV to 550 keV precipitating into the dayside polar ionosphere is observed for the first time by the HEP instrument onboard the RockSat-XN sounding rocket under geomagnetically quiet condition (AE ≤100 nT) at Andøya, Norway. The observed energy spectrum of precipitating electrons follows a power law of -4.86 and the electron flux does not vary much over the observation period (~274.4 seconds). A few minutes before the RockSat-XN observation, POES18 / MEPED observed precipitating electrons, which suggest chorus wave activities at the location close to the rocket trajectory. A ground-based VLF receiver observation at Lovozero, Russia also supports the presence of chorus waves during the rocket observation. A test-particle simulation for wave-particle interactions based on the Arase satellite data shows a similar energy spectrum of precipitating electrons, consistent with the RockSat-XN observation. These results suggest that the precipitation observed by RockSat-XN is likely to be caused by the wave-particle interactions between chorus waves and sub-relativistic electrons.

Plain Language Summary

Sub-relativistic electrons precipitating into the Earth's dayside polar ionosphere are observed by a sounding rocket under geomagnetically quiet conditions. An energy spectrum of these electrons in an energy range from 180 keV to 550 keV is, for the first time, reported. A possible mechanism for generating this precipitation is indicated as a resonance scattering of electrons by chorus waves, based on satellite, ground-based observations, and a test particle simulation.

1 Introduction

Precipitation of sub-relativistic or relativistic electrons is often observed in the auroral ionosphere of the Earth [e.g. *Clilverd et al.*, 2006; *Dietrich et al.*, 2010; *Lorentzen et al.*, 2001; *Blake et al.*, 1996; *Kurita et al*., 2016]. It is suggested that this phenomenon is related to the loss mechanism of the outer radiation belt electrons such as pitch angle scattering due to magnetospheric plasma waves [*Horne & Thorne*, 2003; *Kennel & Petscheck*, 1966]. Such electron precipitation is observed in the nightside and dawnside ionosphere with auroral activities. Besides, precipitation of sub-relativistic or relativistic electrons occurs also on the dayside ionosphere, even when it is quiet. The SAMPEX satellite observed microbursts of the relativistic electron precipitation with a time scale of less than 1 second when AE was less than 100 nT and its peak occurrence rate of one microburst is every 18.9 min at L = 5.5 and ~10 MLT [*Douma et al.*, 2017]. The POES satellites also observed > 30 keV electron precipitation at AE ≤ 100 nT and its peak is the magnetic pre-noon sector [*Lam et al.*, 2010]. However, there are no direct observations of the energy spectra of the precipitating electrons at the dayside ionosphere under the quiet condition, and most of the features of these precipitations have not been understood yet. Characteristic features of the energy spectra of precipitating sub-relativistic or relativistic electrons in the dayside ionosphere, such as slopes of the energy spectra provide important information to verify the relationship between the precipitations and the loss mechanism of the outer radiation belt electrons by comparison with numerical simulations [e.g. *Miyoshi et al., 2015a*].

The dayside sub-relativistic or relativistic electron precipitation may be associated with processes that drive daytime auroral activities [e.g. *Kurita et al., 2015*]. The diffuse aurora is commonly observed from the morning to noon sector at the equatorward edge of the auroral oval and has been considered to originate from the precipitation of tens of keV electrons [*Sandholt et al.*, 2002; *Newell et al.*, 2009], which is driven by a chorus wave in the magnetosphere [*Li et al.*, 2009; *Ni et al.*, 2011a, 2011b, 2014; *Shi et al.*, 2012; *Nishimura et al.*, 2013]. However, there have been few studies about dayside diffuse aurora and their characteristics have not been well understood. For example, they occur actively when the magnetic activity is low as Kp = 0, and some of them occur with pulsation [*Han et al.*, 2015].

In this paper, we report on the first in-situ observation of an energy spectrum of sub-relativistic electrons precipitating into the dayside polar ionosphere made by the RockSat-XN sounding rocket experiment. The rocket was launched under the geomagnetically quiet condition. We also analyze data from the low-altitude POES satellite and ground-based VLF antenna data, which can be used for a proxy of the chorus waves. We also perform a computer simulation for wave-particle interactions and compare calculated energy spectra with the RockSat-XN observations.

We describe the instrumental setup in the next section, which is followed by observational results in Sections 3 and 4. Discussion and summary are provided in Sections 5 and 6, respectively.

2 Instrumentation

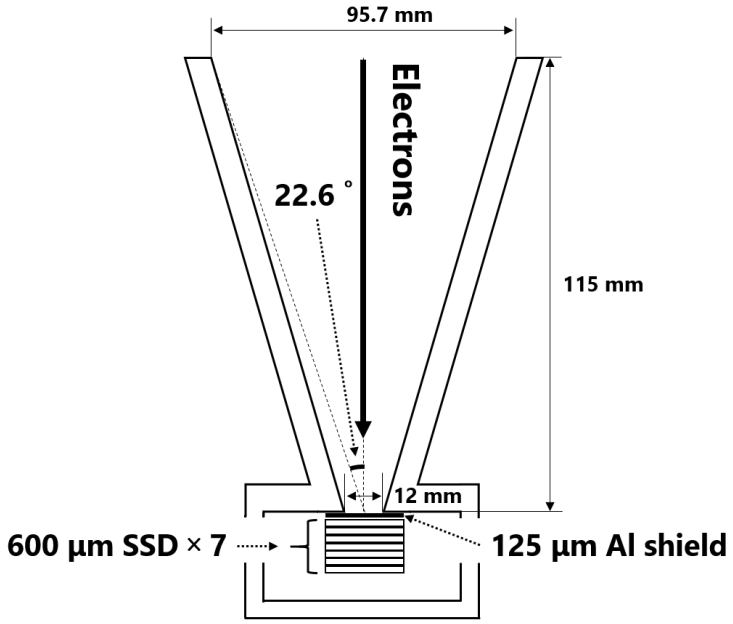

Figure 1. Schematic view of the High Energy Particle (HEP) detector onboard the RockSat-XN sounding rocket. A sample trajectory of an incoming electron is shown.

The RockSat-XN mission is an international student rocket program led by NASA and Colorado Space Grant Consortium (COSGC). It carried 8 observation packages. One of the packages is called PARM (Pulsating AuroRa and Microburst) [*Sugo et al.*, 2020] which includes a high-

energy electron detector (HEP: High Energy Particle detector) and a magnetometer (AFG: ASIC-based FluxGate magnetometer). Pitch angles of observed electrons were calculated by using AFG data in this study.

HEP was designed to measure energy spectra of electrons with energies ranging from 300 keV to 2 MeV. This sensor consists of a mechanical collimator and seven-layered silicon semiconductor detectors (SSDs) which measure energies of incident particles. Figure 1 shows the schematic view of HEP. The thickness of each SSD is 600 μm leading to the total thickness of all the SSDs of 4.2 mm. The SSDs of this thickness enable us to measure the electron's energy up to 1.7 MeV, according to the ESTAR web-database of electron stopping powers and ranges, which is provided by the National Institutes of Standards and Technology (NIST). The field of view of HEP is 22.6° × 22.6° as geometrically defined by the center of the aluminum shield and the edge of the collimator. A 125 μm-thick aluminum sheet was installed just in front of the SSDs, to block electrons with energies less than 300 keV. As a result, 18 % and 70 % of electrons pass through the sheet in the cases of 200 keV and 300 keV electrons, respectively. HEP was mounted on the top of the rocket in such a way that the center of the field of view of HEP was parallel to the thrust axis of the rocket. The pulse height of output signals generated by each SSD layer was digitized by analog-to-digital converters in parallel and sent to the ground.

Figure 2 shows electron energy spectra obtained by the ground calibrations when HEP is irradiated by monoenergetic electron beams. HEP can measure electrons between 300 keV and 2 MeV with energy resolution higher than 22 % (ΔE/E, full width at half maximum). Table 1 summarizes the performance and specifications of HEP. Note that the signal processing time of HEP for each particle detection event is ~ 5 μs.

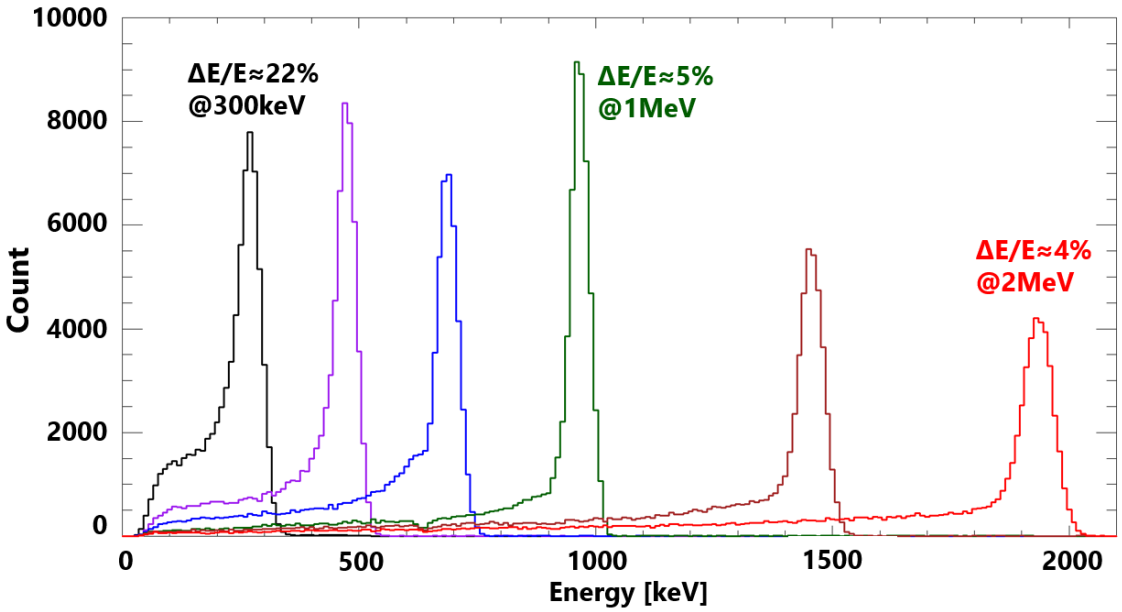

Figure 2. The electron energy spectra measured by HEP under the irradiation of monoenergetic electron beams (300, 500, 700 keV, 1, 1.5, 2 MeV). The total count for each energy spectra is equal.

Table 1. Performance and specifications of HEP.

Parameter	Value
Energy range	300 keV–2 MeV
Energy resolution (ΔE/E)	22%(FWHM) at 300 keV, 5%(FWHM) at 1 MeV
Field of view	22.6° × 22.6° pyramid
Geometric factor	0.81 cm^2 sr
Time resolution	Each event is time-tagged with 100 ns resolution
Mass	2.7 kg
Power	6.7 W (28V × 0.24 A)

3 Observation

RockSat-XN was launched from Andøya Space Center, Norway (69.3°N, 16.0°E in the geographic, 67.4°N 112.3°E in the geomagnetic coordinate system) at 09:13:00 UT on January 13, 2019. Figure 3 (a) shows the position of the launch site and the rocket trajectory. The apex altitude of the trajectory was 184.1 km at 219.6 s from the launch. HEP measured incident particles between 99.6s and 374s from the launch, which correspond to altitudes of 117.2 km at upleg and 73.2 km at downleg, respectively. During the flight, HEP detected 4493 events in total. The zenith angle of the center of the field of view of HEP was between 21.9° and 33.7° from the local magnetic field. The center of the field of view of HEP pointed toward the direction of local pitch angles between 33.8° and 45.5°. Since the field of view of HEP is 22.6° × 22.6°, the observed event includes the electrons with pitch angles between 11.2° and 68.1°.

Figure 3 (b) shows altitude profiles of electron density measured by the EISCAT VHF radar located in Tromsø, Norway (69.60° N, 19.20° E in geographic, and 67.20° N 115.25° E in the geomagnetic coordinate system) on January 13, 2019. The radar pointed to the vertical direction (an elevation angle of 90°). Note that the density enhancement above an altitude of 150 km after 8 UT was due to the photo-ionization caused by the sunlight. There was a weak enhancement of electron density at altitudes above 85 km although the geomagnetic condition during the observation was relatively quiet (AE index was less than 100 nT from 9 UT to 10 UT).

Unfortunately, no satellite was located right on the geomagnetic field line passing through the rocket during the observation. However, there are ground-based and satellite-based observations that suggest the possible appearance of the chorus waves on the field line passing through the rocket. Figure 3 (c) shows precipitating electron fluxes with energies higher than 30 keV observed by the 0-deg. telescope of POES18 / MEPED [*Evans & Greer*, 2000]. Here, an energy channel with central energy of 40 keV (the blue line of Figure 3 (c)) corresponds to electrons with energies higher than 30 keV. MEPED observed electron precipitation from 09:10:20 UT to 09:13:40 UT during which POES18 passed close to Andøya as indicated by the red line of Figure 3 (a). Precipitating electron fluxes with energies higher than 30 keV observed by MEPED can be used as a proxy for the power of chorus waves occurring at the magnetically conjugate locations in the magnetosphere [*Chen et al.*, 2014]. Thus, the observed electron precipitation suggests that

chorus waves were present in the magnetospheric site magnetically connecting to the location of POES18 from 09:10:20 UT to 09:13:40 UT. While POES18 passed close to Andøya at 1.8 to 1 minute before the start of the RockSat-XN / HEP observation, previous studies showed that dayside chorus wave intensification persists for at least 1.5 hours in the same location [*Keika et al.*, 2012]. This suggests that the chorus wave was present simultaneously with the electron precipitation over Andøya during the RockSat-XN / HEP observation. Note that POES18 had moved to locations at 440 – 2200 km southwest from Andøya during the RockSat-XN / HEP observation (9:14:39.6 UT - 9:19:14 UT), where the observed precipitating electron flux was small. The observed decrease of the precipitating flux at the timing of the RockSat-XN / HEP observation may be due to the spatial distribution of an active region of the chorus waves.

Figure 3 (d) shows the frequency-time spectrogram of magnetic field fluctuations obtained by the VLF receiver at Lovozero in Russia. The latitudinal and longitudinal differences between Andøya and Lovozero are 4° and 14° respectively in the geomagnetic coordinate system. The hiss and bursty VLF emissions were observed from 9:10 UT to 9:20 UT, coinciding with the RockSat-XN / HEP observations, and the daytime chorus wave was observed from 9:20 UT to 10:00 UT after the launch. It has been demonstrated that the dayside uniform magnetic field zone can be a source region of dayside chorus waves especially under steady solar wind and quiet geomagnetic conditions [*Keika et al.*, 2012]. The dayside uniform magnetic field zone (DFZ) is the transition region between the near-Earth dipole zone and the compressed, off-equatorial double-minimum field configuration closer to the magnetopause (called the dayside outer zone [*Tsurutani et al.*, 2009]) and distributed over a wide MLT range on the dayside of the magnetosphere. The presence of chorus waves at Lovozero may support the possible appearance of chorus waves in the magnetosphere magnetically connected to Andøya.

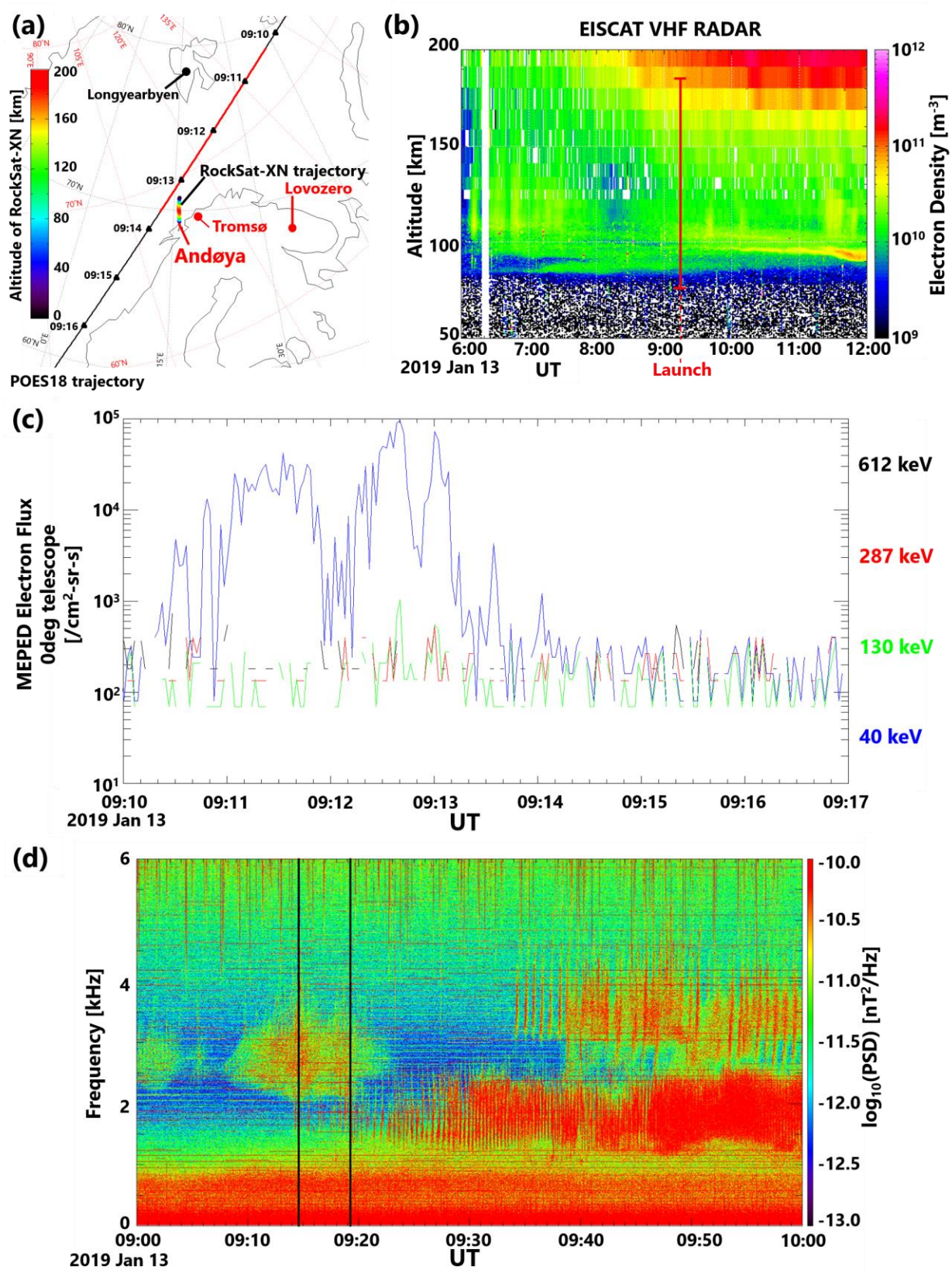
(a)
Altitude of RockSat-XN [km]
200
160
120
80
40
0
Longyearbyen
09:10
09:11
09:12
09:13
09:14
09:15
09:16
RockSat-XN trajectory
Lovozero
Tromsø
Andøya
POES18 trajectory
(b)
EISCAT VHF RADAR
Altitude [km]
200
150
100
50
6:00
7:00
8:00
9:00
10:00
11:00
12:00
2019 Jan 13
UT
Launch
Electron Density [m-3]
10^12
10^11
10^10
10^9
(c)
MEPED Electron Flux
0deg telescope
[/cm2-sr-s]
10^5
10^4
10^3
10^2
10^1
612 keV
287 keV
130 keV
40 keV
09:10
09:11
09:12
09:13
09:14
09:15
09:16
09:17
2019 Jan 13
UT
(d)
Frequency [kHz]
6
4
2
0
09:00
09:10
09:20
09:30
09:40
09:50
10:00
2019 Jan 13
UT
log10(PSD) [nT2/Hz]
-10.0
-10.5
-11.0
-11.5
-12.0
-12.5
-13.0

176

Figure 3. (a) Trajectories of RockSat-XN and POES18, and the locations of Andøya, Lovozero, Tromsø, and Longyearbyen. The color on the RockSat-XN trajectory indicates altitude. The time (UT) shown along the POES18 trajectory indicates the position of the satellite. The red line on POES18 orbit corresponds to the period when the electron precipitation is observed (9:10:20 UT to 9:13:40 UT). (b) Electron density around the launch measured by EISCAT VHF radar at Tromsø. The red line indicates the launch time, and the solid line part corresponds to the altitude observed by the RockSat-XN sounding rocket. (c) Fluxes of precipitating electrons observed by the 0-deg. telescope of POES18 / MEPED. Energy labels of the precipitating electrons are center energies of each energy channel of MEPED obtained using the bow tie method [*Green*, 2013b] and 40 keV (blue), 130 keV (green), 287 keV (red), and 612 keV (black). (d) Frequency-time spectrogram of plasma waves observed at Lovozero. The interval between the two black lines corresponds to the period of the RockSat-XN observation.

Error! Reference source not found. (a, black line) shows an energy spectrum of particles detected by HEP from 99.6 s to 374 s from the launch. Here the energy is the sum of deposited energies in all SSDs. The detected energy of incident particles ranges from ~50 keV to ~30 MeV with two peaks at 130 keV and 1.5 MeV. The raw observation data contain background noise such as Galactic Cosmic Rays (GCRs) and electrons originated from Cosmic Ray Albedo Neutron Decay (CRAND). Therefore, we have to evaluate and then remove these noises components from the data. In the next section, we describe how we remove the noises due to GCRs and CRAND.

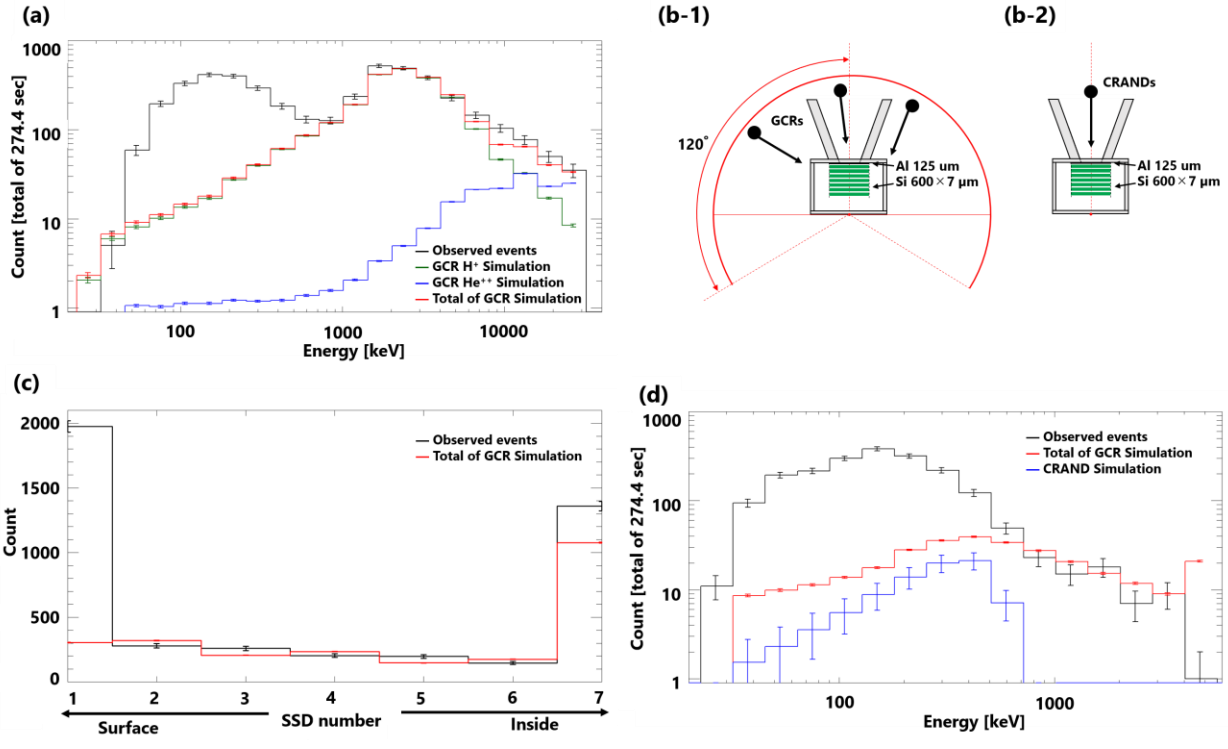

Figure 4. (a) The energy spectra of all observed events (Black), simulation results of Background Galactic Cosmic Ray (GCR) protons (Green), alpha particles (Blue), and the sum of them (Red).

The incident flux of GCR is calculated by the model of Lal [1985] (ϕ = 300 MeV). (b) Setup of the numerical simulations for estimating the noise level due to GCR and CRAND. (b-1) GCR protons and alpha particles were injected isotropically from the region of polar angles from 0° to 120° on a spherical surface (3π sr). (b-2) A pencil beam of electrons is injected toward the center of SSDs vertically for the simulation of CRAND. (c) The histogram of the number of SSD layer in which particles (black: the observation, red: the estimated GCR particles) deposit their energies more than 31 keV. Counts of the seventh SSD layer includes penetrating particles. (d) The energy spectra of (black) observed events, the estimated background (red) GCR protons and alpha particles, and (blue) CRAND electrons which deposit energies only on the first SSD layer.

4 Noise reduction and estimation of precipitating electron energy spectra

4.1 Noise reduction due to GCR

We investigated the energy spectra of galactic cosmic ray protons and alpha particles using the models of Castagnoli & Lal [1980], which have a parameter ϕ indicating the influence of modulation due to solar activity. To estimate the background noise due to GCR, we calculate the response of HEP to GCRs with the Geant4 toolkit [*Agostinelli et al.*, 2003; *Allison et al.*, 2006: *Allison et al.*, 2016]. A schematic view of the simulation setup is shown in Figure 4 (b-1)**Error! Reference source not found.**. Here, GCR particles were assumed to be uniformly injected from an area with a solid angle of 3π sr (see Figure 4 (b-1)). Since GCRs are shielded by the earth, we assume that GCRs do not enter HEP from the bottom.

The green and blue lines in Figure 4 (a) show the estimated energy spectra of GCR protons and alpha particles detected by HEP during the observation period. These spectra are calculated by the numerical simulations with the model parameter ϕ of GCR as 300 MeV. The red line in Figure 4 (a) shows the sum of the blue and green lines. As evident from the figure, the higher energy component (> 1 MeV) of the observed spectrum is consistent with the estimated noise spectrum due to GCR. On the other hand, the estimated GCR counts are significantly smaller than the observed particle counts in the energy range between 40 keV and several hundred keV.

Figure 4 (c) shows histograms of the number of hit SSDs. Here, the hit threshold is set to 31 keV for energy deposit at each layer. To evaluate particles that seem to be appropriate as incidents from the collimator, these histograms includes only particles that sequentially hit from the first layer SSD. For example, we excluded particles that do not hit on the first layer and those which hit on the first and third layers but not on the second from these histograms. The excluded particles account for only 1.6 % of the total number observed. Most of the observed particles stop at the first SSD layer or reach the seventh layer (black line). The latter cases are consistent with that of estimated galactic cosmic ray protons and alpha particles (red line) since most of them deposit their energies on all the SSD layers and their energies are very high. However, the former feature cannot be explained by GCRs. In the following analysis, we deal with only particles that stopped in the first SSD layer since the other components are consistent with the noise level due to GCRs. Note that we subtract the estimated proton and alpha particles counts which deposit energies only on the first layer from observed particle counts.

4.2 Noise reduction due to CRAND

An electron flux due to CRAND is estimated by integrating the spatial distribution of the electron production rate due to neutron decay [*Hess et al.*, 1961] along the trajectory of electrons with an equatorial pitch angle of 1.6° which corresponds to the average center of the field of view of HEP for the dipole magnetic field line passing through Andøya (L= 6.77). Details of this calculation are shown by Lencheck et al. [1961]. Here, we integrate the electron production rate from the altitude of 100 km in the southern hemisphere to the altitude of 100 km in the northern hemisphere. We consider the electrons in the loss cone. The noise due to CRAND electrons is then estimated by a Geant4 calculation with the electron fluxes of the CRAND origin. The simulation setup is briefly shown in Figure 4 (b-2)**Error! Reference source not found.**. We consider CRAND electrons to enter HEP in the normal direction of SSDs. The blue line in Figure 4 (d) shows the estimated energy spectrum observed by HEP due to CRAND, where we select particles that deposited their energies more than 31 keV only on the first SSD layer. The estimated counts due to CRAND are much smaller than those detected during the observation.

Finally, we evaluate the energy spectrum of electrons of the magnetospheric origin by subtracting the GCR protons, alpha particles, and CRAND electron counts shown in Figure 4 (d) from the observed counts. The electron flux can be measured up to the maximum value of the energy bin for which significant counts remain after subtracting the GCRs and CRAND electrons. The subtracted flux indicates that the observed particles with energies less than 500 keV may contain precipitating electrons generated by plasma processes in the magnetosphere.

4.3 Estimation of the energy spectrum of precipitating electrons

To obtain an energy spectrum of the precipitating electron flux, we need to consider instrumental effects such as the aluminum shield located just in front of SSDs (see Figure 1), and electrons which deposit their energies partially and run away from the first SSD layer. Figure 5 shows the estimated probability distribution of detected energies at the first SSD layer as a function of incident electron energy in the case that the particles deposit their energies only on the first SSD layer, as calculated by the Geant4 toolkit. Incident electrons with monochromatic energy are detected as electrons with energies lower than the incident energy following certain probability distribution. The total detection efficiency is ≤ 10 % for ≤ 180 keV electrons and 1 % for ≤ 150 keV. It is thus difficult to discuss the incident energy spectrum of electrons below 180 keV. Electrons with 550 keV that enter HEP are most likely to be observed as 500 keV, which is the maximum value of the electron energy detected in this observation, as discussed above. Therefore, we consider that the effective energy range of the present observation is from180 keV to 550 keV.

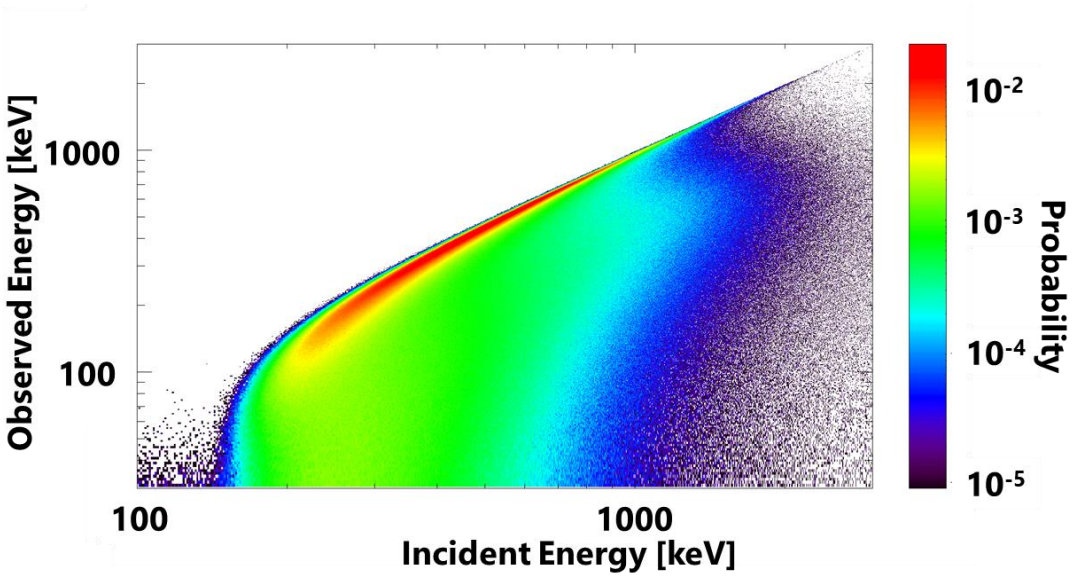

Figure 5. The probability distribution of detected energies as a function of incident electron energies deposited on the first SSD layer only. Uncertainty of detected energies coming from the energy resolution of HEP is taken into account.

The black line in Figure 6 (a) shows the energy-spectrum of observed electrons where signals above 31 keV are detected only by the first SSD layer during 99.6 s to 374 s from the launch. The number of the detected electrons in the *i*-th energy bin f_i (the index *i* denotes the energy bin number) is given by a product of the energy spectrum of the incident electrons s_j (the index *j* denotes the energy bin number of the incident electrons) and a matrix of the probability distribution of the HEP detector response R_{ij}, as follows;

$$f_i = \sum_j R_{ij} s_j. \quad (1)$$

The matrix element R_{ij} is the probability that an incident electron in the *j*-th energy bin is detected in the *i*-th energy bin. We assumed that s_j follows power-law form Ax^B, where *x* is incident energy, A and B are parameters to be estimated. We derived a coefficient A and exponent B of the power-law model that minimizes chi-square with Levenberg-Marquardt least-squares method [*Press et al.*, 1992]. Here, the chi-square is calculated as the sum of the squares of the differences between the number of the electrons detected by HEP in the RockSat-XN observation f_i^{obs} and that calculated from the model incident spectrum $f_i^{model} = \sum_j R_{ij} s_j$ divided by the measurement error of f_i^{obs}.

The red line in Figure 6 (b) shows the estimated energy spectrum of incident electrons s_j that give the minimum chi-square, and the blue line in Figure 6 (a) shows f_i^{model} corresponding to the red line s_j.

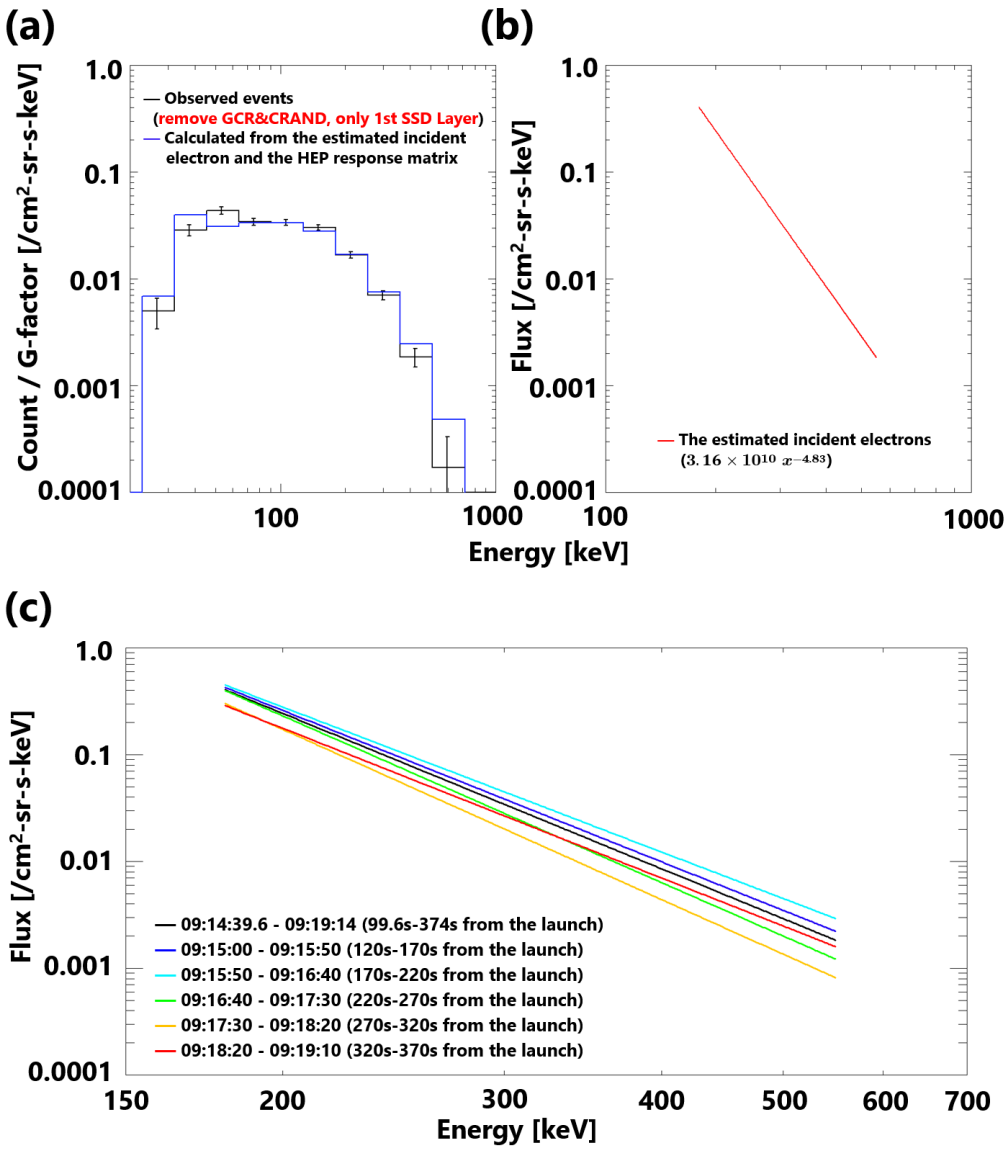

Figure 6. (a) The energy spectrum obtained by removing GCRs and CRAND electrons from the particles deposited only on the first SSD layer f_i^{obs} (black) and the energy spectrum calculated from the incident electron spectrum and the HEP response matrix f_i^{model} (blue). (b) The estimated energy spectrum of incident electrons s_j that denotes $3.16 \times 10^{10}\ x^{-4.83}$ ($\chi^2 = 35.0$). (c) Energy spectra of incident electrons calculated every 50 seconds. Their fluctuations are ± 30 % and ± 60 % at 180 keV and 550 keV, respectively. Note that the black line shows the energy spectra averaged from 99.6 s to 374 s from launch (same as the red line in Figure 6 (b)).

Figure 6 (c) shows the energy spectra of incident electrons s_j estimated every 50 s, starting from 120s after launch. The black line in Figure 6 (c)**Error! Reference source not found.** is the estimated s_j averaged from 99.6 s to 374 s from launch (same as the red line in Figure 6 (b)). These calculated electron fluxes are more or less stable in time, where fluctuations are ± 30 % and ± 60 % at 180 keV and 550 keV, respectively.

5 Discussion

In the RockSat-XN experiment, we have observed a significant number of sub-relativistic electrons precipitating into the dayside polar ionosphere with energies of several hundred keV under the quiet magnetospheric condition. A likely explanation for these electrons is pitch angle scattering of electrons in the dayside magnetosphere due to wave-particle interactions with chorus waves, which are evident from the complementary ground and satellite observations during the RockSat-XN observation (Figure 3 (c, d)). Chorus waves can interact with high-energy electrons when they propagate to high latitude because the resonance energy increases with increasing the background magnetic field strength [*Horne & Thorne*, 2003, *Miyoshi et al.*, 2010, 2015a]. The equatorial chorus wave amplitude distribution for AE ≤ 100 nT is highest in the dawn MLT sector (7–13 MLT) [*Li et al*., 2009] and these dayside chorus waves show little dependence of occurrence on geomagnetic activity [*Tsurutani & Smith*, 1977; *Spasojević & Inan*, 2010]. Also, Bunch et al. [2012] showed that the time-averaged chorus wave power in the dayside outer magnetosphere can exceed 10 pT for latitudes up to 45° off the equator.

In addition to the present observations, we estimate the flux of sub-relativistic electron precipitation by using a computer simulation about wave-particle interactions (GEMSIS-RBW [*Saito et al.*, 2012]). In the simulation, electron precipitation is caused by pitch-angle scattering of magnetospheric electrons by chorus waves. Synthesized chorus wave packets are given at the magnetic equator and propagate toward the high latitude along the dipole geomagnetic field. For the source magnetospheric electron population in this simulation, we used an energy - pitch angle distribution of electron flux observed by the HEP instrument [*Mitani et al.*, 2018] on board the Arase satellite [*Miyoshi et al.*, 2018b]. The energy - pitch angle distribution, which is given for each satellite spin (~8 s), was averaged between 9:00 UT and 9:30 UT on January 13, 2019, during which the Arase satellite was located at L* = 5.57 - 5.50 and MLT = 18.21 – 18.52. Here, L* is the value of L shell defined by Roederer [1970]. Although Arase was located on the duskside, the difference in L* between Andøya (L* = 6.23) and Arase locations are only 0.66 – 0.73. Note that the angular resolution of Arase / HEP is larger than the local loss cone angle of electrons at Arase. We thus used observed electron flux in the pitch angle bin covering 0 – 11.25° as a flux just outside the loss cone. In case of lack of data for that pitch angle bin, the flux value was extrapolated from the other bins of the same energy by assuming that the pitch angle distribution follows a cosine function. In this simulation, we modeled the rising tones of chorus waves with an amplitude of magnetic fluctuations as 17 pT based on POES18 / MEPED observations [*Chen et al.*, 2014] and a frequency band of 0.2 – 0.5 $|\Omega_e|$ based on the VLF measurement at Lovozero (Figure 3 (c)), where Ω_e is the electron cyclotron frequency. The background magnetic field strength at the magnetic equator is set as 125 nT by using the TS05 model [*Tsyganenko and Sitnov.*, 2005], and the background electron density in the magnetosphere is set as 3.78 cm^{-3} based on the model by Sheeley et al. [2001]. Furthermore, we assume that the chorus waves propagate up to the magnetic latitude of 40° along the field line, where the resonance energy of electrons with the chorus waves with a frequency of 0.3 $|\Omega_e|$ is 640 keV at L* = 6.23. The repetition period of each chorus element is set as 3 Hz which is a typical modulation period of chorus waves [e.g., *Miyoshi et al.*, 2015a].

A simulated energy spectrum of precipitating electrons is shown with the red line in Figure 7. It shows a similar spectrum profile with the RockSat-XN / HEP observation in the energy range from 200 keV to 500 keV. The absolute values of electron flux by the GEMSIS-RBW simulation shows good agreement with those of the RockSat-XN / HEP observation despite their different MLT positions. These results strongly support the interpretation that the sub-relativistic electron precipitation observed by RockSat-XN is generated through pitch angle scattering of magnetospheric electrons with the chorus waves.

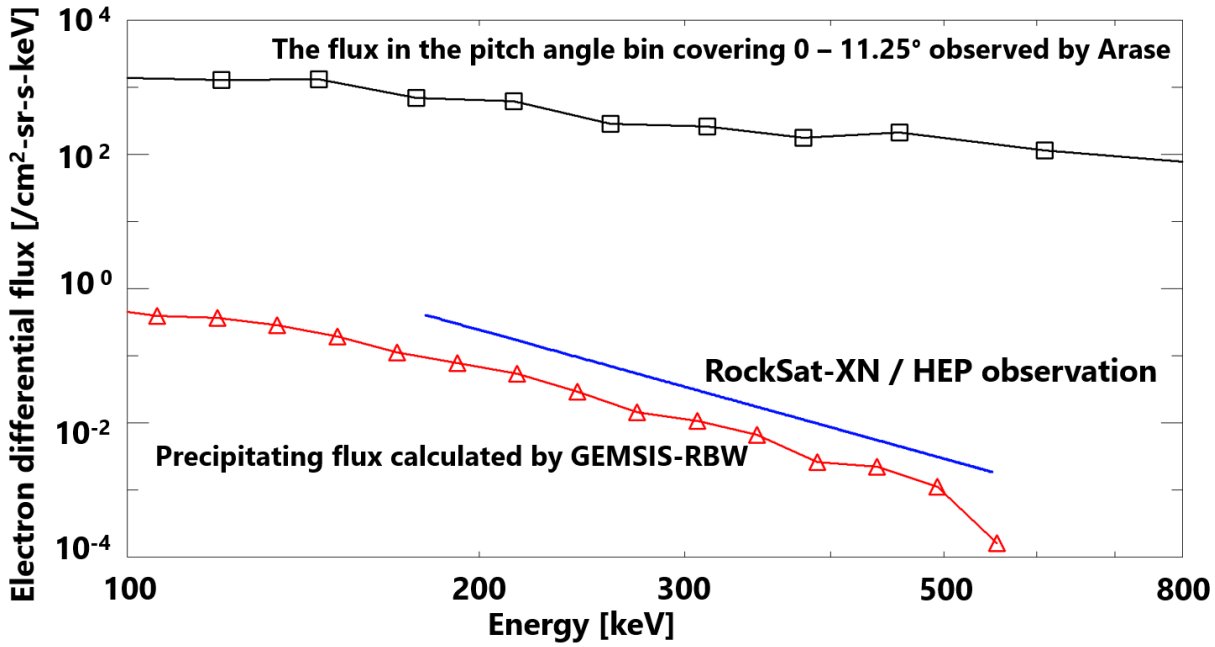

Figure 7. Energy spectra of electrons precipitating into the ionosphere. The flux (blue) observed by RockSat-XN / HEP and (red) calculated by GEMSIS-RBW simulation using the electron measurement by Arase satellite. The black line shows the electron energy spectrum in the pitch angle bin covering 0 – 11.25° of the energy - pitch angle distribution of electron flux observed by RockSat-XN / HEP and that calculated by GEMSIS-RBW simulation have a similar power-law index.

Both electron precipitations observed by POES18 / MEPED and RockSat-XN / HEP may be related to dayside pulsating/diffuse auroral activity. POES18 / MEPED observed electron precipitation from 72.6°N to 68.4°N in the geomagnetic coordinate system. On the other hand, the dayside pulsating aurora was observed at Longyearbyen (Figure 3 (a)), located at 75.1°N in the geomagnetic coordinate system until 8 UT. Auroral emission was not detected due to the cloudy weather after 8 UT, but dayside pulsating aurora activity was not surprising to be present during the RockSat-XN / HEP observation because the dayside pulsating aurora frequently occurs at 8-13 MLT [*Han et al.*, 2015]. Since the electron precipitation observed by POES18 continued up to the region close to Andøya, there may be also pulsating/diffuse auroral activity at Andøya during the RockSat-XN / HEP observation. The speculation is also supported by the continuous increase of electron density at altitudes between 80 and 110 km measured with the

EISCAT VHF radar in Tromsø. The speculation also suggests the possible relationship between the dayside pulsating/diffuse auroral activity and chorus waves since both electron precipitations observed by POES18 and RockSat-XN may be related to dayside chorus waves.

The sub-relativistic electron microbursts occur with a peak occurrence rate at L = 5.5 and ~10 MLT on the dayside ionosphere at AE ≤ 100 nT [*Douma et al.*, 2017] and one of the possible mechanisms for generating microburst is pitch angle scattering of electrons due to wave-particle interactions [*Horne & Thorne*, 2003; *Hikishima et al.*, 2010]. Furthermore, their relationship to pulsating auroras has been suggested [*Saito et al.*, 2012, *Miyoshi et al*., 2015a, b]. These features may also be present in the sub-relativistic electrons observed by RockSat-XN / HEP. However, we were unable to discriminate the temporal characteristics of the microbursts less than 1 second because the observed particle count rates of RockSat-XN / HEP was not sufficient.

6 Conclusion

The energy spectrum of precipitating electrons in the sub-relativistic energy range, from 180 keV to 550 keV, in the quiet dayside auroral ionosphere has been obtained by in-situ observation by RockSat-XN / HEP for the first time. The energy spectrum of the observed precipitation follows a power law of -4.86 and temporal variations of the fluxes are ± 30 % and ± 60 % at 180 keV and 550 keV, respectively.

A few minutes before the RockSat-XN observation, POES18 / MEPED observed precipitating electrons related to the power of chorus waves at the location close to Andøya. The VLF receiver observation at Lovozero also supports the presence of chorus waves during the RockSat-XN / HEP observation. Furthermore, the GEMSIS-RBW simulation using Arase satellite data as input parameters shows an energy spectrum of precipitating electrons in good agreement with that observed by RockSat-XN. All of the observations and the simulation suggest that the precipitation observed by RockSat-XN was caused by the wave-particle interactions between chorus waves and sub-relativistic electrons and was also likely to be accompanied by dayside pulsating/diffuse auroras.

Acknowledgments, Samples, and Data

We are grateful for the support of NASA Wallops Flight Facility's (WFF) and Andøya Space Center (ASC). This research was financially supported by the Grants-in-Aid for Scientific Research (15H05815, 15H05747, 16H06286, 17H00728, 18KK0100, 20H01959, 20H01955) by the Ministry of Education, Science, Sports and Culture, Japan. This study was supported by JSPS Bilateral Open Partnership Joint Research Projects. We thank Dr. Janet Green and the NOAA's National Geophysical Data Center (NGDS) for providing NOAA data. The rocket and instruments' data used in this study are available at the UTokyo Repository (http://hdl.handle.net/2261/00079467). The data of the VLF receiver are available at the site (http://aurora.pgia.ru/erg-pgi/case1.html). The AE index used in this paper was provided by the WDC for Geomagnetism, Kyoto (http://wdc.kugi.kyoto-u.ac.jp/wdc/Sec3.html). The magnetic

coordinate system is calculated by the IGRF-13 model (https://www.ngdc.noaa.gov/IAGA/vmod/igrf.html). EISCAT is an international association supported by research organizations in China (CRIRP), Finland (SA), Japan (NIPR and ISEE), Norway (NFR), Sweden (VR), and the United Kingdom (UKRI). The EISCAT data used in this study are processed with the help of the EISCAT staff and published on the web (http://pc115.seg20.nipr.ac.jp/www/eiscatdata/). Science data of the ERG (Arase) satellite were obtained from the ERG Science Center (ERG-SC) operated by ISAS/JAXA and ISEE/Nagoya University (https://ergsc.isee.nagoya-u.ac.jp/index.shtml.en, Miyoshi et al., 2018a). The present study analyzed MGF-L2 v03_03 data, HEP-L2 v03_01 data, and orbit L3 v02 data obtained by ERG. Part of the work of YM and TH was done at ERG-SC. The present study used SPEDAS for data analysis [*Angelopoulos et al*., 2019]

References

Agostinelli, S., Allison, J., Amako, K., Apostolakis, J., Araujo, H., Arce, P., et al. (2003). GEANT4 - A simulation toolkit. *Nuclear Instruments and Methods in Physics Research, Section A: Accelerators, Spectrometers, Detectors and Associated Equipment*, *506*(3), 250–303. https://doi.org/10.1016/S0168-9002(03)01368-8

Allison, J., Amako, K., Apostolakis, J., Araujo, H., Dubois, P. A., Asai, M., et al. (2006). Geant4 developments and applications. *IEEE Transactions on Nuclear Science*, *53*(1), 270–278. https://doi.org/10.1109/TNS.2006.869826

Allison, J., Amako, K., Apostolakis, J., Arce, P., Asai, M., Aso, T., et al. (2016). Recent developments in GEANT4. *Nuclear Instruments and Methods in Physics Research, Section A: Accelerators, Spectrometers, Detectors and Associated Equipment*, *835*, 186–225. https://doi.org/10.1016/j.nima.2016.06.125

Angelopoulos, V., Cruce, P., Drozdov, A., Grimes, E. W., Hatzigeorgiu, N., King, D. A., et al. (2019). The Space Physics Environment Data Analysis System (SPEDAS). Space Science Reviews (Vol. 215). The Author(s). https://doi.org/10.1007/s11214-018-0576-4

Blake, J. B., Looper, M. D., Baker, D. N., Nakamura, R., Klecker, B., & Hovestadt, D. (1996). New high temporal and spatial resolution measurements by SAMPEX of the precipitation of relativistic electrons. *Advances in Space Research*, *18*(8), 171–186. https://doi.org/10.1016/0273-1177(95)00969-8

Bunch, N. L., Spasojevic, M., & Shprits, Y. Y. (2012). Off-equatorial chorus occurrence and wave amplitude distributions as observed by the Polar Plasma Wave Instrument. *Journal of Geophysical Research: Space Physics*, *117*(4), 1–14. https://doi.org/10.1029/2011JA017228

Castagnoli, G., & Lal, D. (1980). Solar Modulation Effects in Terrestrial Production of Carbon-14. *Radiocarbon*, *22*(2), 133–158. https://doi.org/10.1017/s0033822200009413

Chen, Y., Reeves, G. D., Friedel, R. H. W., & Cunningham, G. S. (2014). Global time-dependent chorus maps from low-Earth-orbit electron precipitation and Van Allen Probes data. *Geophysical Research Letters*, *41*(3), 755–761. https://doi.org/10.1002/2013GL059181

Clilverd, M. A., Rodger, C. J., & Ulich, T. (2006). The importance of atmospheric precipitation in storm-time relativistic electron flux drop outs. *Geophysical Research Letters*, *33*(1), 1–5. https://doi.org/10.1029/2005GL024661

Dietrich, S., Rodger, C. J., Clilverd, M. A., Bortnik, J., & Raita, T. (2010). Relativistic microburst storm characteristics: Combined satellite and ground-based observations. *Journal of Geophysical Research: Space Physics*, *115*(12), 1–10. https://doi.org/10.1029/2010JA015777

Douma, E., Rodger, C. J., Blum, L. W., & Clilverd, M. A. (2017). Occurrence characteristics of relativistic electron microbursts from SAMPEX observations. *Journal of Geophysical Research: Space Physics*, *122*(8), 8096–8107. https://doi.org/10.1002/2017JA024067

Evans, D. S., & Greer, M. S. (2000). Polar orbiting environmental satellite space environment monitor - 2: Instrument descriptions and archive data documentation, *NOAA Technical Memorandum*, Boulder, Colorado OAR SEC 93, 93, version 1.4, January 2004.

Green, J. C. (2013a). External users manual, POES/MetOp SEM-2 processing, version 1.0, 20., *NOAA National Geophysical Data Center*. Available at http://www.ngdc.noaa.gov/stp/satellite/poes/documentation.html.

Green, J. C. (2013b). MEPED Telescope Data Processing Algorithm Theoretical Basis Document, version 1.0, 77., *NOAA National Geophysical Data Center*. Available at http://www.ngdc.noaa.gov/stp/satellite/poes/documentation.html.

Han, D., Chen, X., Liu, J., Qiu, Q., Keika, K., Hu, Z., et al. (2015). An extensive survey of dayside diffuse aurora based on optical observations at Yellow River Station. *Journal of Geophysical Research: Space Physics*, *120*(9), 7447–7465. https://doi.org/10.1002/2015JA021699

Hess, W. N., Canfield, E. H., & Lingenfelter, R. E. (1961). Cosmic-ray neutron demography. *Journal of Geophysical Research*, *66*(3), 665–677. https://doi.org/10.1029/jz066i003p00665

Hikishima, M., Omura, Y., & Summers, D. (2010). Microburst precipitation of energetic electrons associated with chorus wave generation. *Geophysical Research Letters*, *37*(7), 1–5. https://doi.org/10.1029/2010GL042678

Horne, R. B., & Thorne, R. M. (2003). Relativistic electron acceleration and precipitation during resonant interactions with whistler-mode chorus. *Geophysical Research Letters*, *30*(10), 3–6. https://doi.org/10.1029/2003gl016973

Keika, K., Spasojevic, M., Li, W., Bortnik, J., Miyoshi, Y., & Angelopoulos, V. (2012). PENGU In/AGO and THEMIS conjugate observations of whistler mode chorus waves in the dayside

uniform zone under steady solar wind and quiet geomagnetic conditions. *Journal of Geophysical Research: Space Physics*, *117*(7), 1–15. https://doi.org/10.1029/2012JA017708

Kennel, C. F., & Petschek, H. E. (1966). Limit on stably trapped particle fluxes. *Journal of Geophysical Research*, *71*(1), 1–28. https://doi.org/10.1029/jz071i001p00001

Kurita, S., Kadokura, A., Miyoshi, Y., Morioka, A., Sato, Y. & Misawa, H. (2015), Relativistic electron precipitations in association with diffuse aurora: Conjugate observation of SAMPEX and the all-sky TV camera at Syowa Station, *Geophysical Research Letters*, 42(12), 4702– 4708. https://doi.org/10.1002/2015GL064564

Kurita, S., Miyoshi, Y., Blake, J. B., Reeves, G. D., & Kletzing, C. A. (2016). Relativistic electron microbursts and variations in trapped MeV electron fluxes during the 8-9 October 2012 storm: SAMPEX and Van Allen Probes observations. *Geophysical Research Letters*, *43*(7), 3017–3025. https://doi.org/10.1002/2016GL068260

Lal, D. (1985). Theoretically Expected Variations in the Terrestrial Cosmic-Ray Production Rates of Isotopes, *Proc. of the Inter. School of Physics*, Course XCV, Solar-Terrestrial Relationships and the Earth Environment in the last Millennia, G. C. Castagnoli ed., 216-233.

Lam, M. M., Horne, R. B., Meredith, N. P., Glauert, S. A., Moffat-Griffin, T., & Green, J. C. (2010). Origin of energetic electron precipitation >30 keV into the atmosphere. *Journal of Geophysical Research A: Space Physics*, *115*(A4), 1–15. https://doi.org/10.1029/2009JA014619

Lenchek, A. M., Singer, S. F., & Wentworth, R. C. (1961). Geomagnetically trapped electrons from cosmic ray albedo neutrons. *Journal of Geophysical Research*, *66*(12), 4027–4046. https://doi.org/10.1029/JZ066i012p04027

Li, W., Thome, R. M., Angelopoulos, V., Bortnik, J., Cully, C. M., Ni, B., et al. (2009). Global distribution of whistler-mode chorus waves observed on the THEMIS spacecraft. *Geophysical Research Letters*, *36*(9), 1–5. https://doi.org/10.1029/2009GL037595

Lorentzen, K. R., Looper, M. D., & Blake, J. B. (2001). Relativistic electron microbursts during the GEM storms. *Geophysical Research Letters*, *28*(13), 2573–2576. https://doi.org/10.1029/2001GL012926

Matsuoka, A., Teramoto, M., Nomura, R., Nosé, M., Fujimoto, A., Tanaka, Y., et al. (2018). The ARASE (ERG) magnetic field investigation. *Earth, Planets and Space*, *70*(1), 1–16. https://doi.org/10.1186/s40623-018-0800-1

Mitani, T., Takashima, T., Kasahara, S., Miyake, W., & Hirahara, M. (2018). High-energy electron experiments (HEP) aboard the ERG (Arase) satellite. *Earth, Planets and Space*, *70*(1), 1–14. https://doi.org/10.1186/s40623-018-0853-1

Miyoshi, Yoshizumi, Katoh, Y., Nishiyama, T., Sakanoi, T., Asamura, K., & Hirahara, M. (2010). Time of flight analysis of pulsating aurora electrons, considering wave-particle

interactions with propagating whistler mode waves. *Journal of Geophysical Research: Space Physics*, *115*(10), 1–7. https://doi.org/10.1029/2009JA015127

Miyoshi, Y., Oyama, S., Saito, S., Kurita, S., Fujiwara, H., Kataoka, R., et al. (2015a). Energetic electron precipitation associated with pulsating aurora: EISCAT and Van Allen Probe observations. *Journal of Geophysical Research: Space Physics*, *120*(4), 2754–2766. https://doi.org/10.1002/2014JA020690

Miyoshi, Y., Saito, S., Seki, K., Nishiyama, T., et al., (2015b). Relation between fine structure of energy spectra for pulsating aurora electrons and frequency spectra of whistler mode chorus waves. *Journal of Geophysical Research: Space Physics*, *120*(9), 7728-7736. https://doi.org/10.1002/2015JA021562

Miyoshi, Yoshizumi, Hori, T., Shoji, M., Teramoto, M., Chang, T. F., Segawa, T., et al. (2018a). The ERG Science Center. *Earth, Planets and Space*, *70*(1). https://doi.org/10.1186/s40623-018-0867-8

Miyoshi, Yoshizumi, Shinohara, I., Takashima, T., Asamura, K., Higashio, N., Mitani, T., et al. (2018b). Geospace exploration project ERG. *Earth, Planets and Space*, *70*(1). https://doi.org/10.1186/s40623-018-0862-0

Newell, P. T., Sotirelis, T., & Wing, S. (2009). Diffuse, monoenergetic, and broadband aurora: The global precipitation budget. *Journal of Geophysical Research: Space Physics*, *114*(9), 1–20. https://doi.org/10.1029/2009JA014326

Ni, B., Thorne, R. M., Shprits, Y. Y., Orlova, K. G., & Meredith, N. P. (2011a). Chorus-driven resonant scattering of diffuse auroral electrons in nondipolar magnetic fields. *Journal of Geophysical Research: Space Physics*, *116*(6), 1–12. https://doi.org/10.1029/2011JA016453

Ni, B., Thorne, R., Liang, J., Angelopoulos, V., Cully, C., Li, W., et al. (2011b). Global distribution of electrostatic electron cyclotron harmonic waves observed on THEMIS. *Geophysical Research Letters*, *38*(17), 4–8. https://doi.org/10.1029/2011GL048793

Ni, B., Li, W., Thorne, R. M., Bortnik, J., Ma, Q., Chen, L., et al. (2014). Resonant scattering of energetic electrons by unusual low-frequency hiss. *Geophysical Research Letters*, *41*(6), 1854–1861. https://doi.org/10.1002/2014GL059389

Nishimura, Y., Bortnik, J., Li, W., Thorne, R. M., Ni, B., Lyons, L. R., et al. (2013). Structures of dayside whistler-mode waves deduced from conjugate diffuse aurora. *Journal of Geophysical Research: Space Physics*, *118*(2), 664–673. https://doi.org/10.1029/2012JA018242

Press, W. H., Teukolsky, S. A., Vetterling, W. T., Flannery, B. P. (1992). Numerical Recipes in C: The Art of Scientific Computing, Second Edition. *Cambridge: Cambridge University Press*

Roederer, J. G. (1970). Dynamics of Geomagnetically Trapped Radiation. *New York: Springer.* https://doi.org/10.1007/978-3-642-49300-3

574 Saito, S., Miyoshi, Y., & Seki, K. (2012). Relativistic electron microbursts associated with
575 whistler chorus rising tone elements: GEMSIS-RBW simulations. *Journal of Geophysical*
576 *Research: Space Physics*, *117*(10), 1–9. https://doi.org/10.1029/2012JA018020

577 Sandholt, P. E., Denig, W. F., Farrugia, C. J., Lybekk, B., & Trondsen, E. (2002). Auroral
578 structure at the cusp equatorward boundary: Relationship with the electron edge of low-
579 latitude boundary layer precipitation. *Journal of Geophysical Research: Space Physics*,
580 *107*(A9), 1–9. https://doi.org/10.1029/2001JA005081

581 Sheeley, B. W., Moldwin, M. B., Rassoul, H. K., & Anderson, R. R. (2001). An empirical
582 plasmasphere and trough density model: CRRES observations. *Journal of Geophysical*
583 *Research: Space Physics*, *106*(A11), 25631–25641. https://doi.org/10.1029/2000JA000286

584 Shi, R., Han, D., Ni, B., Hu, Z. J., Zhou, C., & Gu, X. (2012). Intensification of dayside diffuse
585 auroral precipitation: Contribution of dayside Whistler-mode chorus waves in realistic
586 magnetic fields. *Annales Geophysicae*, *30*(9), 1297–1307. https://doi.org/10.5194/angeo-30-
587 1297-2012

588 Spasojevic, M., & Inan, U. S. (2010). Drivers of chorus in the outer dayside magnetosphere.
589 *Journal of Geophysical Research A: Space Physics*, *115*(A4), 1–12.
590 https://doi.org/10.1029/2009JA014452

591 Sugo, S., Kawashima, O., Kasahara, S., Asamura, K., Nomura, R., Miyoshi, Y., Energy-resolved
592 detection of precipitating electrons of 30–100 keV by a sounding rocket associated with
593 dayside chorus waves. *Earth and Space Science Open Archive*,
594 https://doi.org/10.1002/essoar.10503830.1

595 Thébault, E., Finlay, C. C., Beggan, C. D., Alken, P., Aubert, J., Barrois, O., et al. (2015).
596 International geomagnetic reference field: The 12th generation international geomagnetic
597 reference field - The twelfth generation. *Earth, Planets and Space*, *67*(1).
598 https://doi.org/10.1186/s40623-015-0228-9

599 Thorne, R. M., O'Brien, T. P., Shprits, Y. Y., Summers, D., & Horne, R. B. (2005). Timescale
600 for MeV electron microburst loss during geomagnetic storms. *Journal of Geophysical*
601 *Research: Space Physics*, *110*(A9), 1–7. https://doi.org/10.1029/2004JA010882

602 Tsurutani, B. T., & Smith, E. J. (1977). Two types of magnetospheric ELF chorus and their
603 substorm dependences. *Journal of Geophysical Research*, *82*(32), 5112–5128.
604 https://doi.org/10.1029/ja082i032p05112

605 Tsurutani, B. T., Verkhoglyadova, O. P., Lakhina, G. S., & Yagitani, S. (2009). Properties of
606 dayside outer zone chorus during HILDCAA events: Loss of energetic electrons. *Journal of*
607 *Geophysical Research: Space Physics*, *114*(3), 1–19. https://doi.org/10.1029/2008JA013353

608 Tsyganenko, N. A., & Sitnov, M. I. (2005). Modeling the dynamics of the inner magnetosphere
609 during strong geomagnetic storms. *Journal of Geophysical Research: Space Physics*,
610 *110*(A3), 1–16. https://doi.org/10.1029/2004JA010798
611

Figure 1.

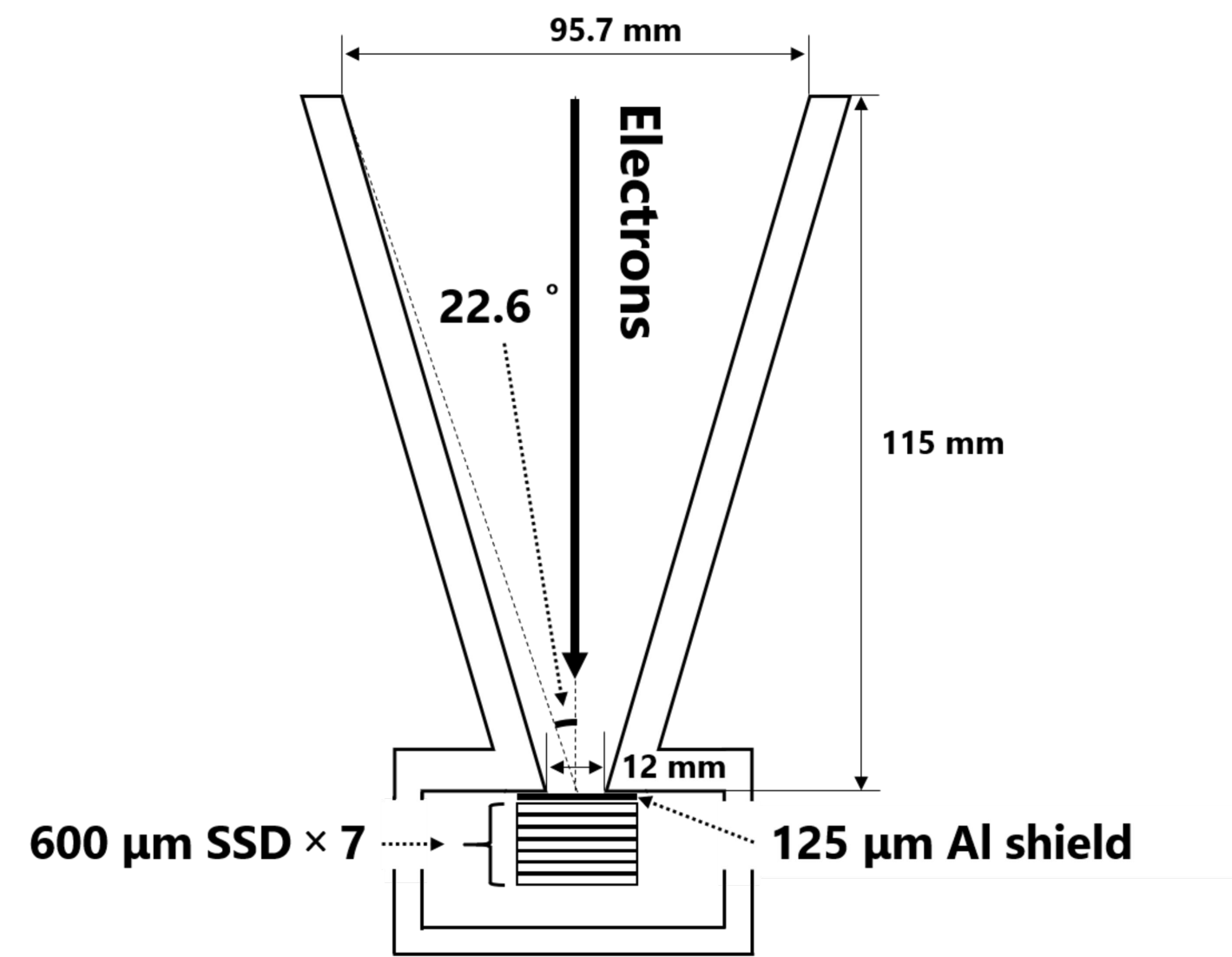
95.7 mm
Electrons
22.6 °
115 mm
12 mm
600 µm SSD × 7
125 µm Al shield

Figure 2.

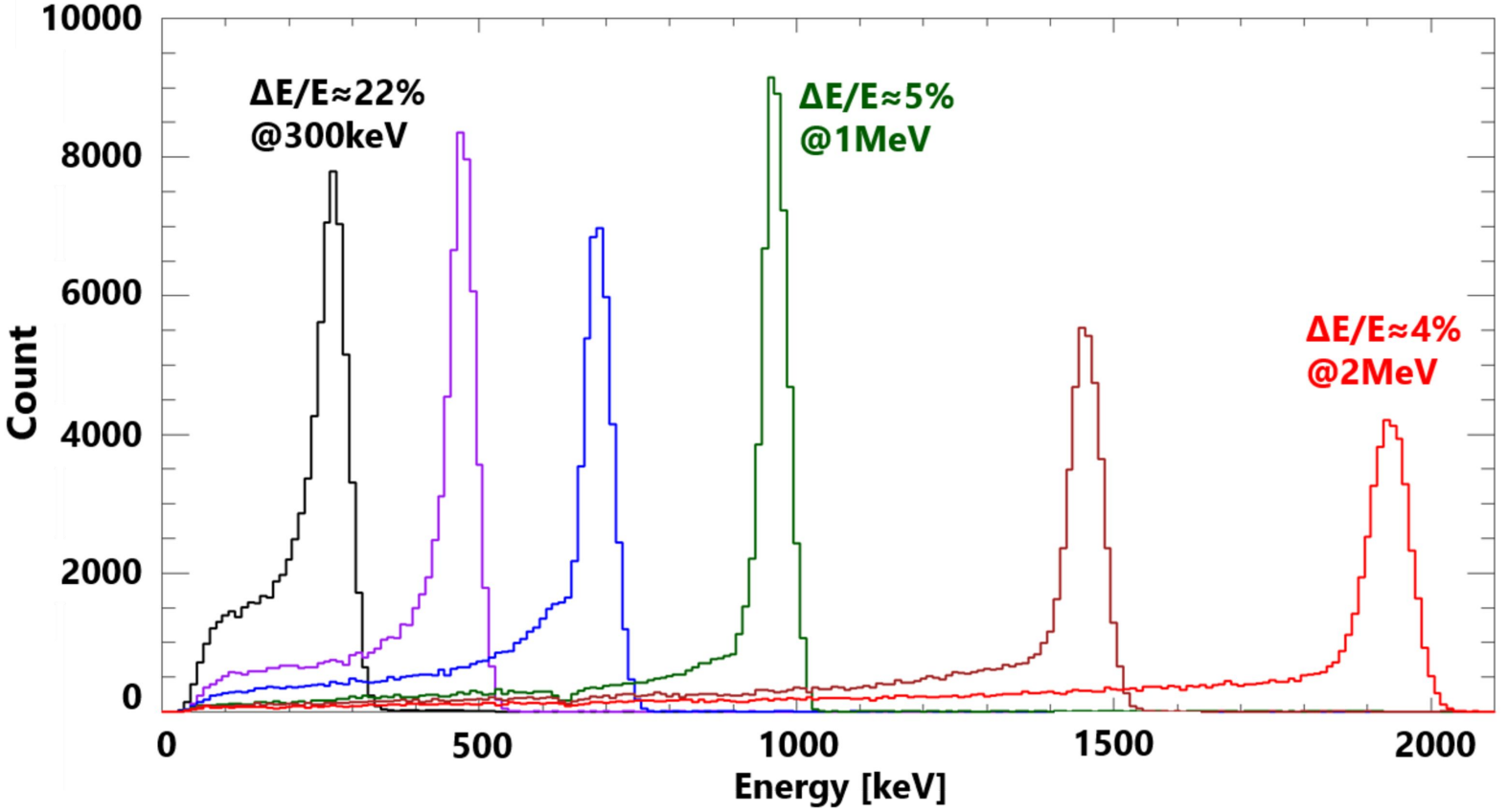
ΔE/E≈22%
@300keV
ΔE/E≈5%
@1MeV
ΔE/E≈4%
@2MeV
Count
Energy [keV]
0
2000
4000
6000
8000
10000
0
500
1000
1500
2000

Figure 3.

(a)

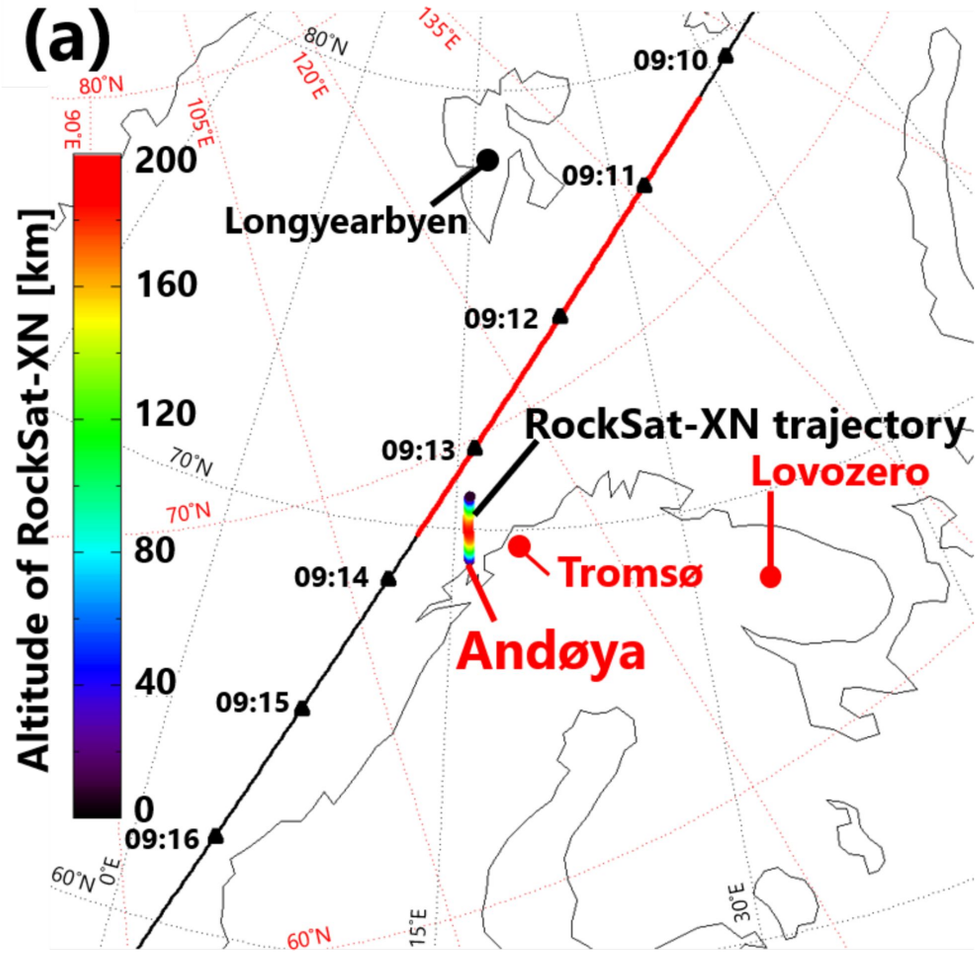

POES18 trajectory

(b)

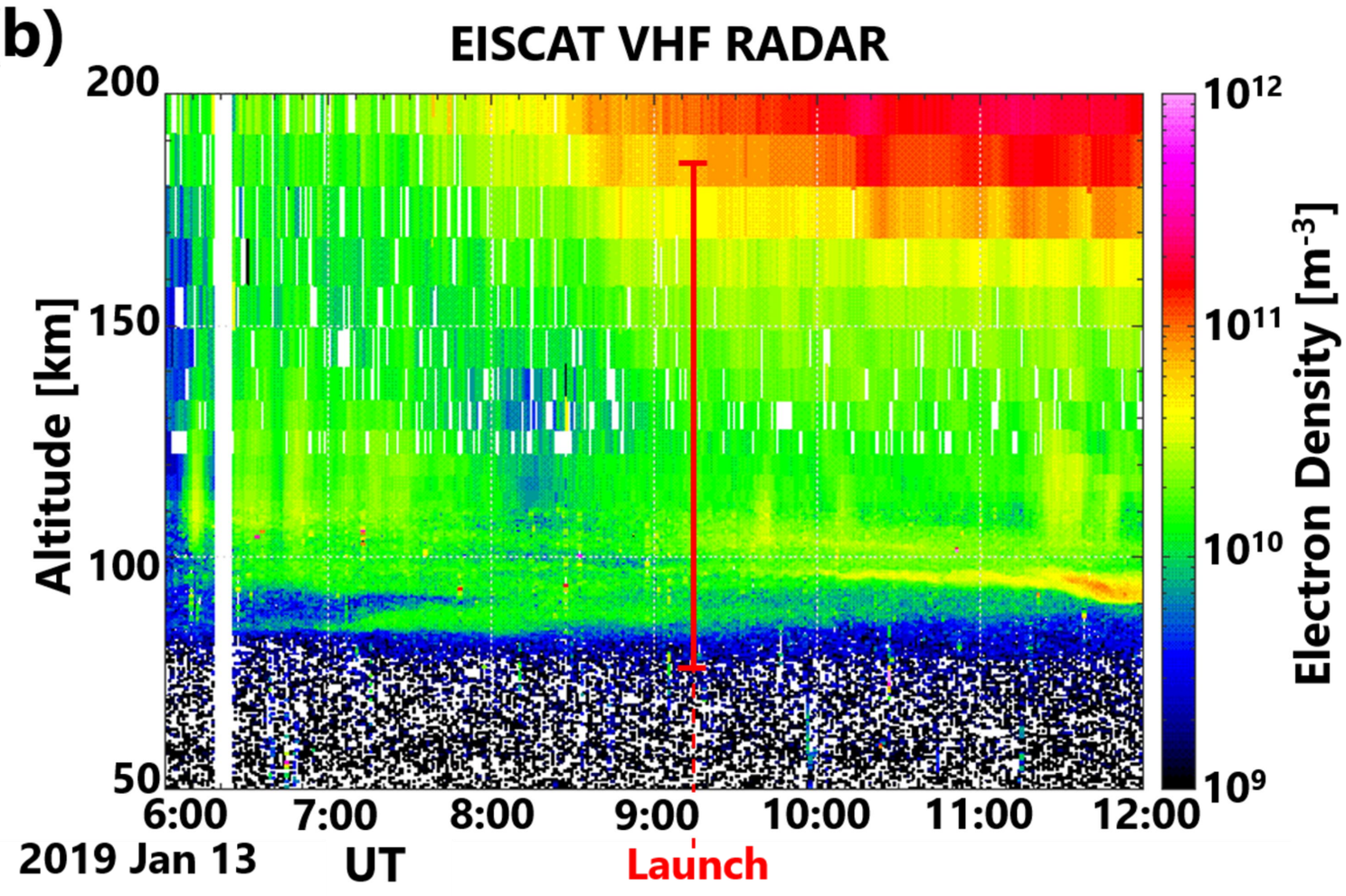

(c)

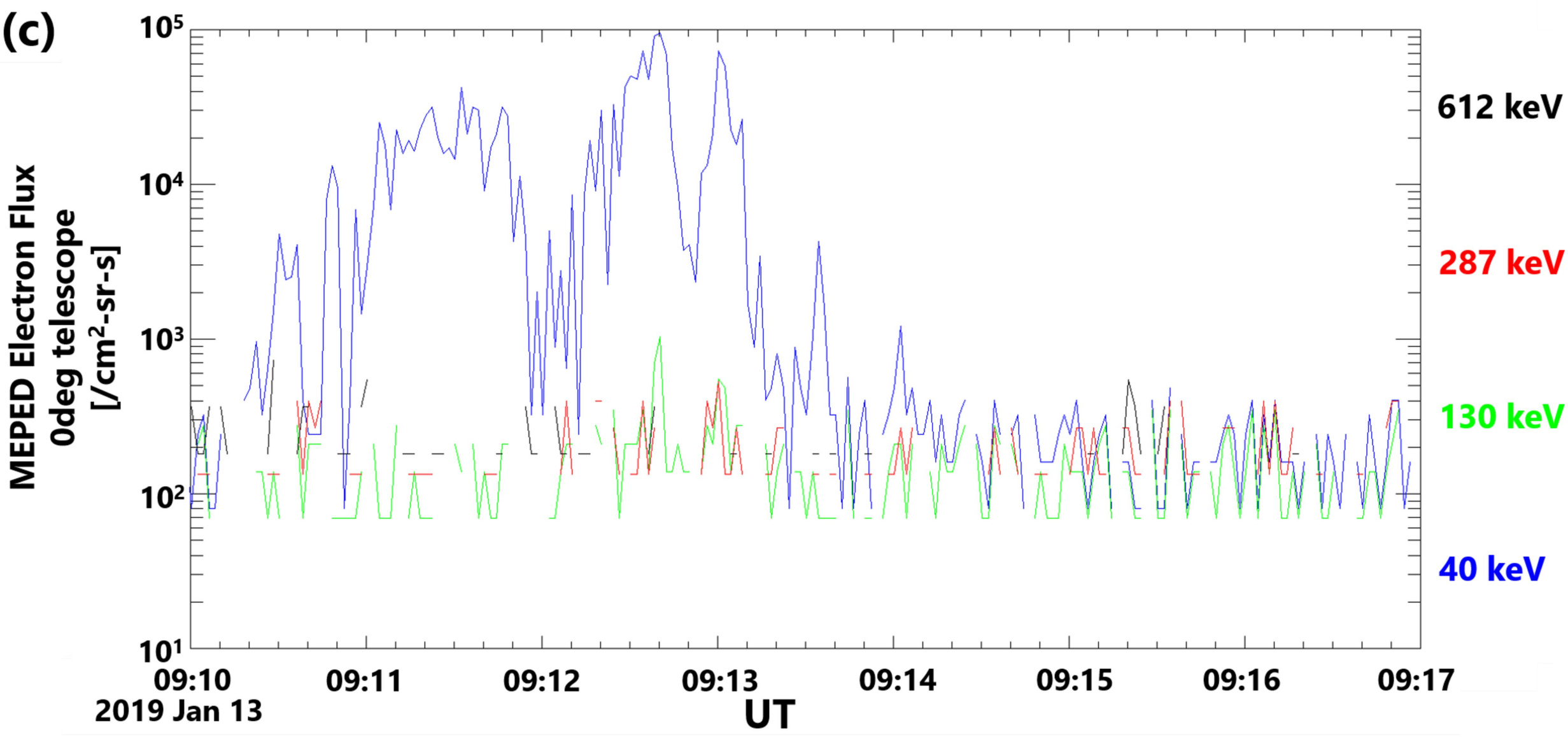

(d)

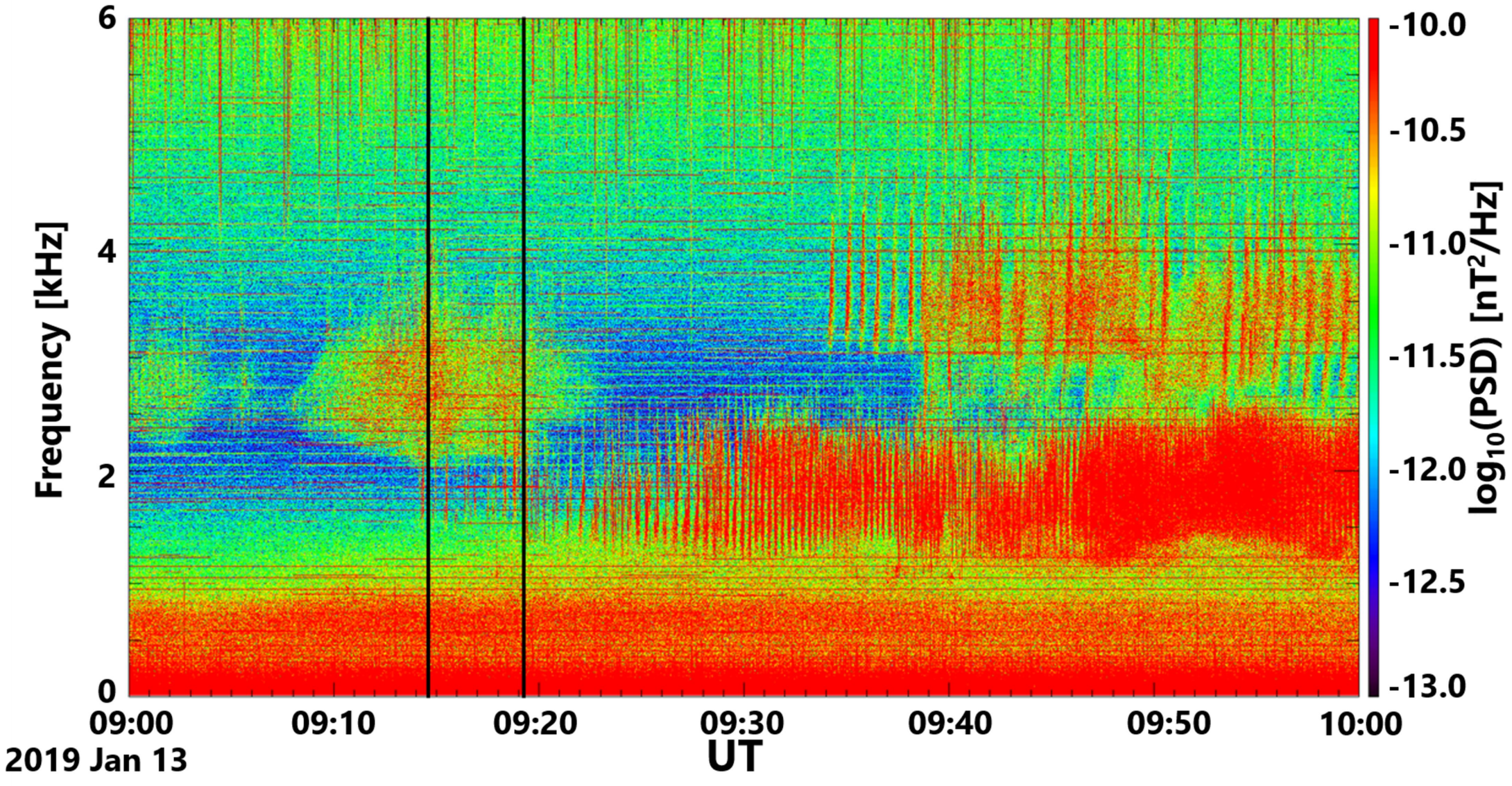

Figure 4.

(a)

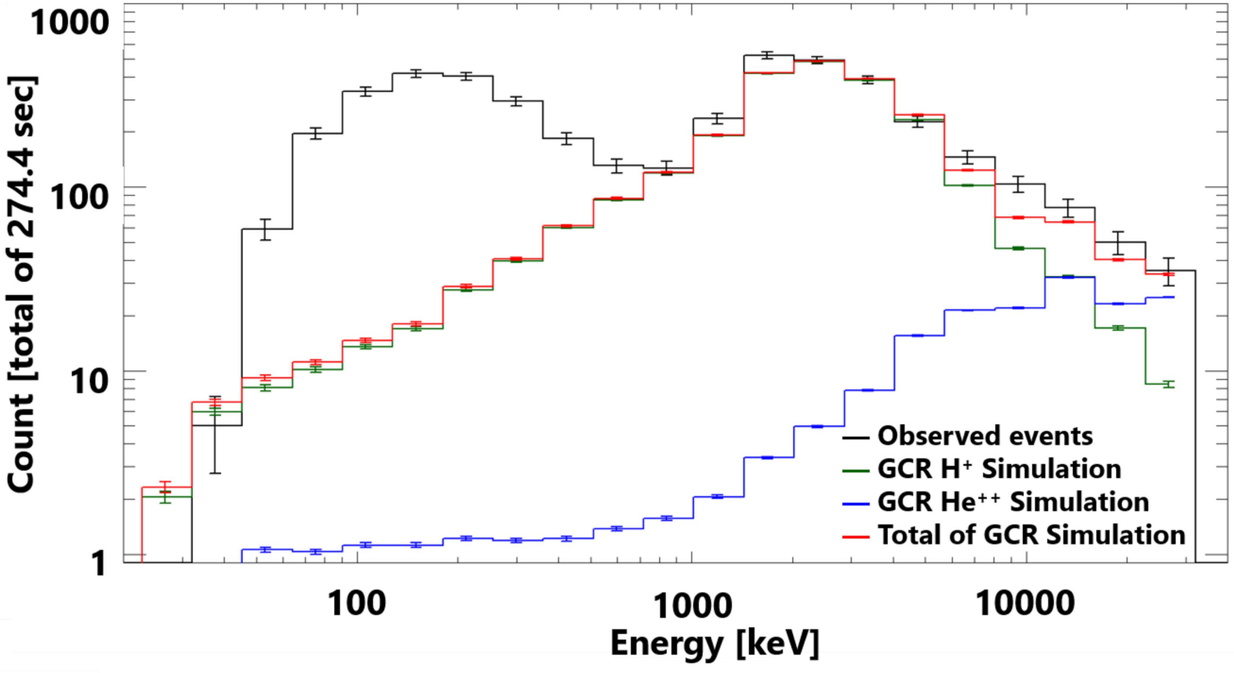
Count [total of 274.4 sec]
1000
100
10
1
100
1000
10000
Energy [keV]
Observed events
GCR H+ Simulation
GCR He++ Simulation
Total of GCR Simulation

(b-1)

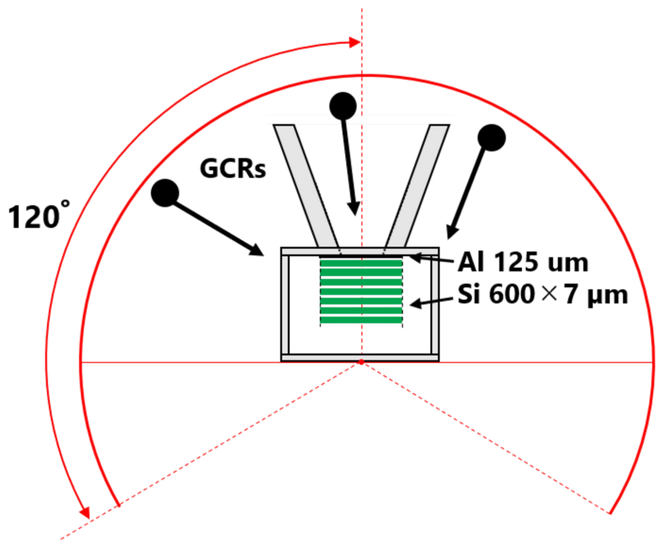
120°
GCRs
Al 125 um
Si 600×7 μm

(b-2)

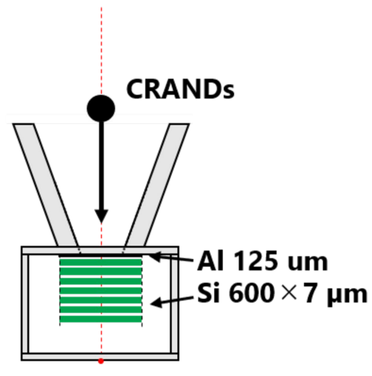
CRANDs
Al 125 um
Si 600×7 μm

(c)

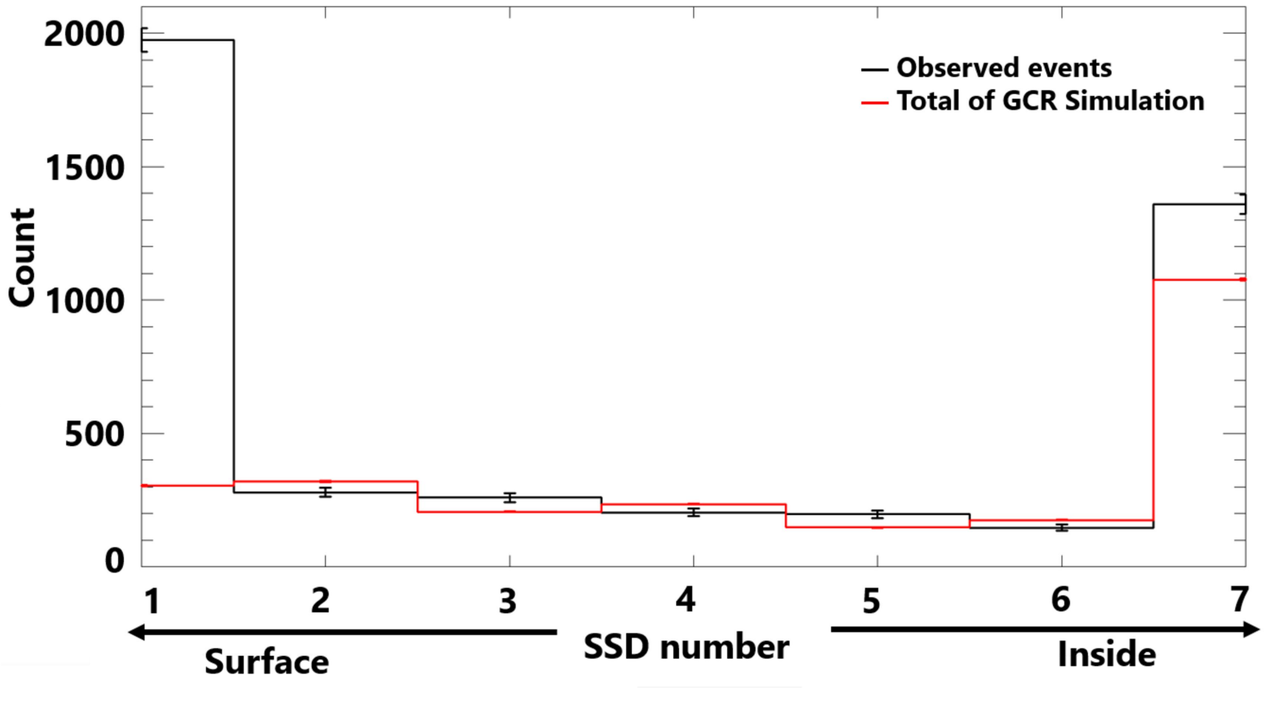
Count
2000
1500
1000
500
0
Observed events
Total of GCR Simulation
1
2
3
4
5
6
7
Surface
SSD number
Inside

(d)

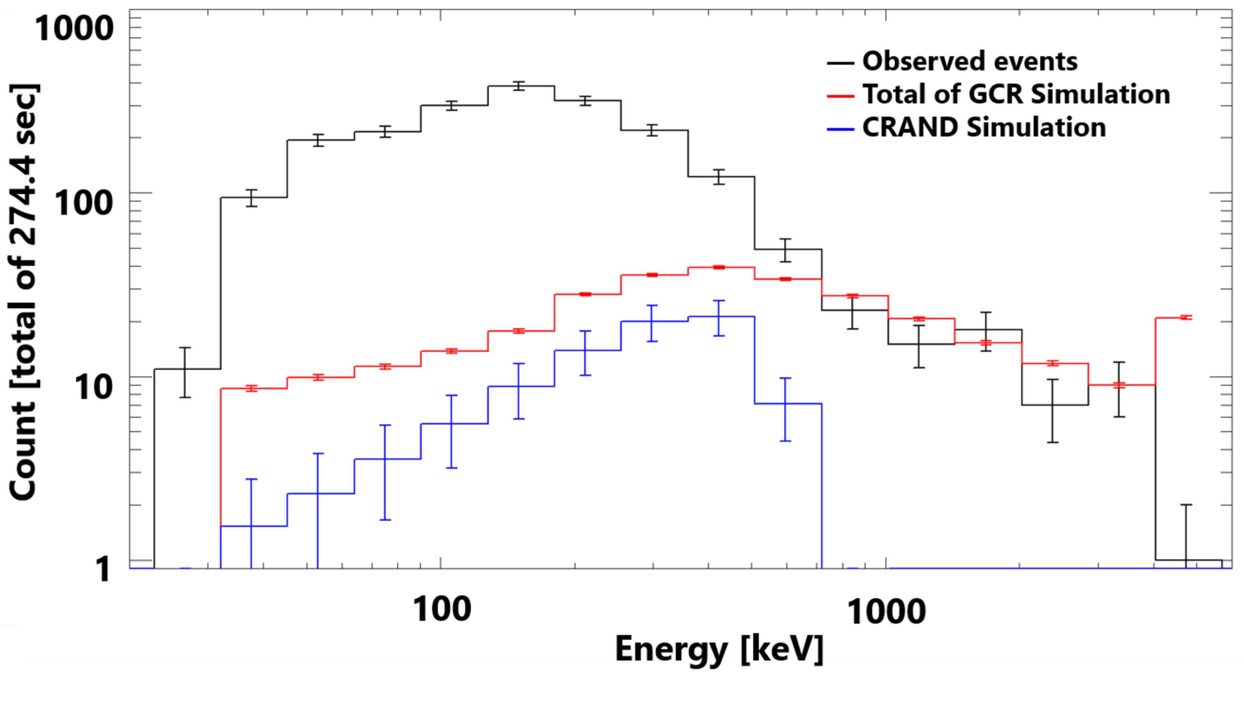
Count [total of 274.4 sec]
1000
100
10
1
Observed events
Total of GCR Simulation
CRAND Simulation
100
1000
Energy [keV]

Figure 5.

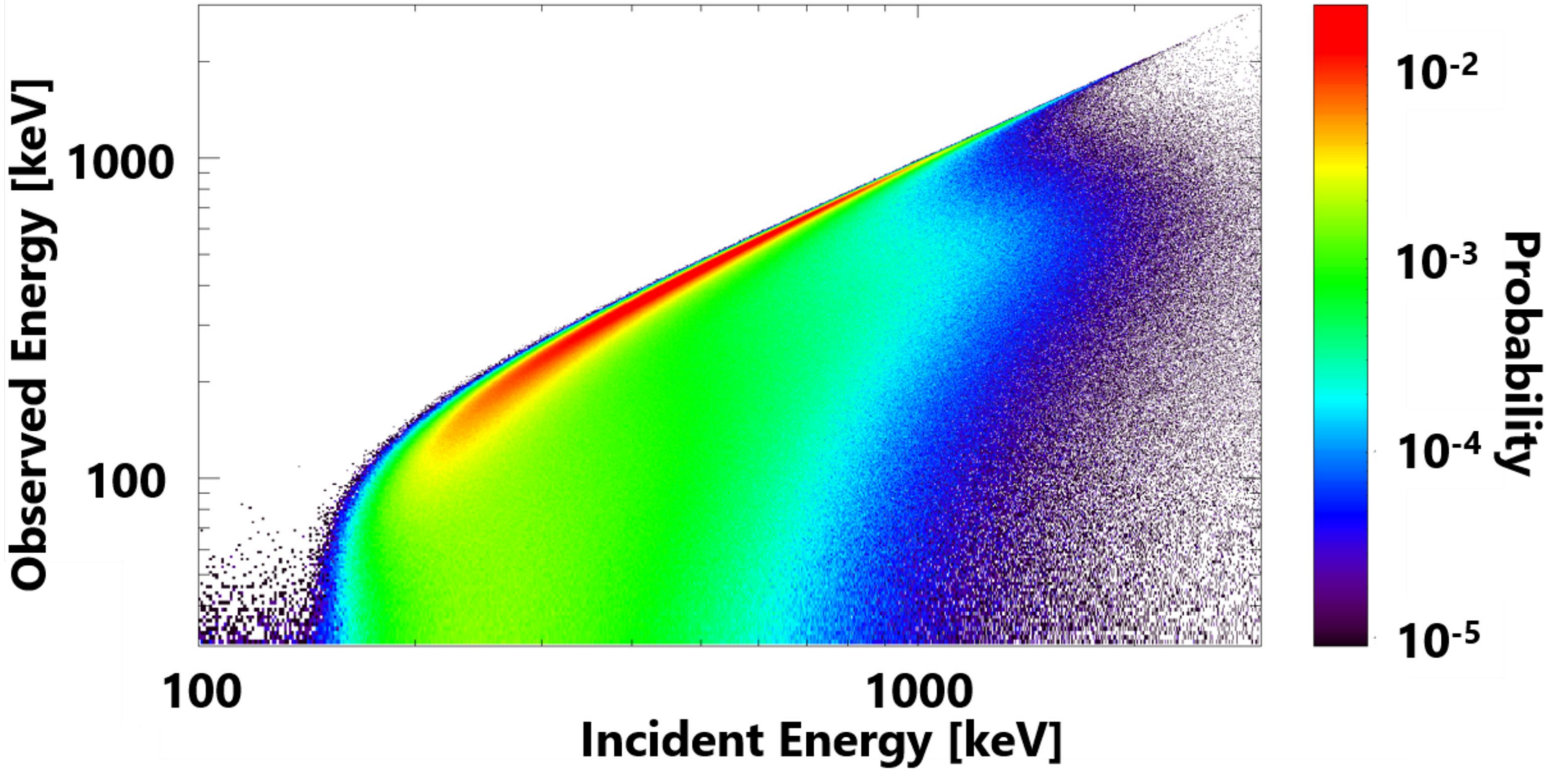
Observed Energy [keV]
1000
100
100
1000
Incident Energy [keV]
10^{-2}
10^{-3}
10^{-4}
10^{-5}
Probability

Figure 6.

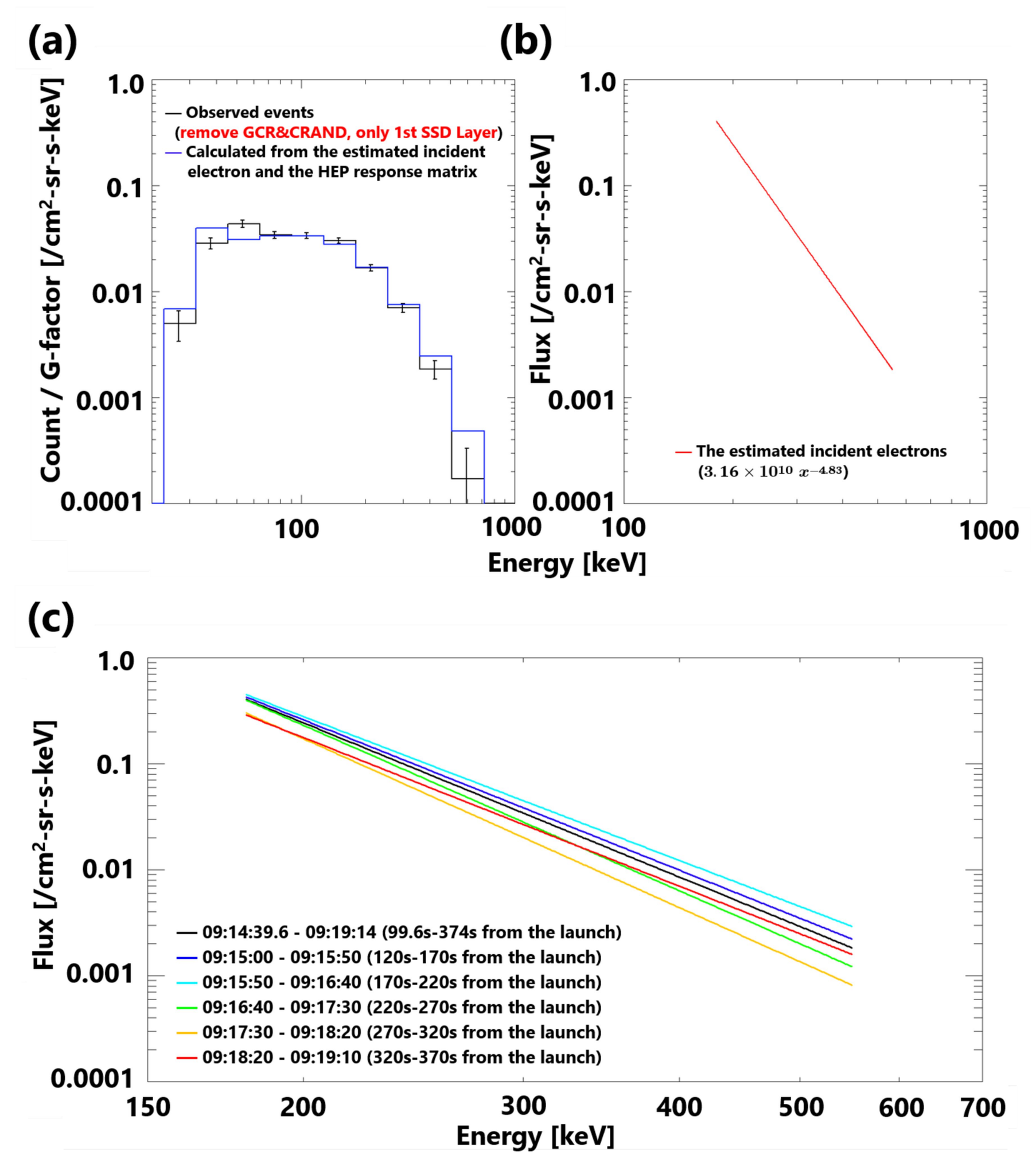
(a)
(b)
(c)
Observed events
(remove GCR&CRAND, only 1st SSD Layer)
Calculated from the estimated incident electron and the HEP response matrix
Count / G-factor [/cm²-sr-s-keV]
Flux [/cm²-sr-s-keV]
The estimated incident electrons
$(3.16 \times 10^{10}\ x^{-4.83})$
Energy [keV]
09:14:39.6 - 09:19:14 (99.6s-374s from the launch)
09:15:00 - 09:15:50 (120s-170s from the launch)
09:15:50 - 09:16:40 (170s-220s from the launch)
09:16:40 - 09:17:30 (220s-270s from the launch)
09:17:30 - 09:18:20 (270s-320s from the launch)
09:18:20 - 09:19:10 (320s-370s from the launch)

Figure 7.

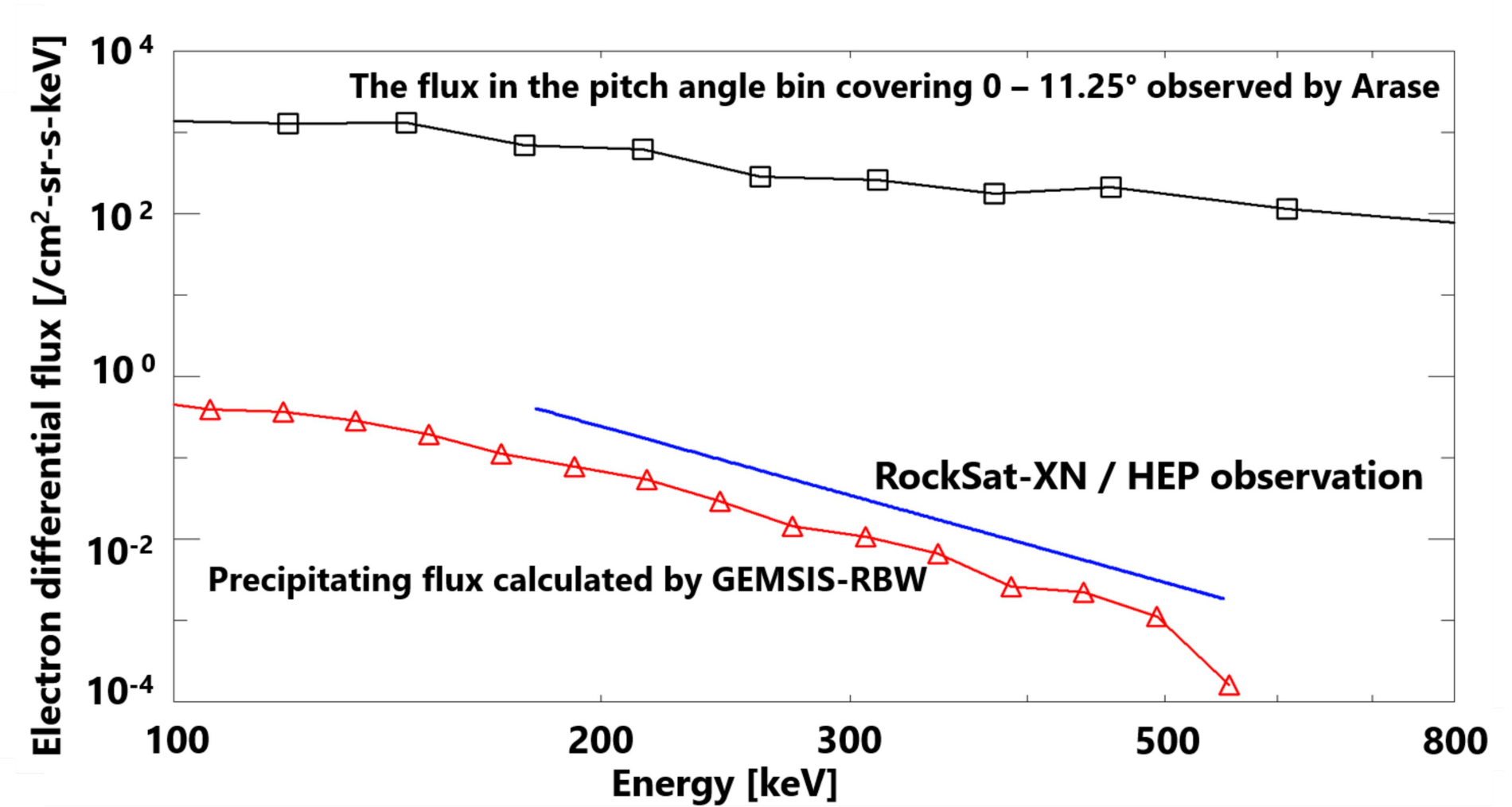
The flux in the pitch angle bin covering 0 – 11.25° observed by Arase
RockSat-XN / HEP observation
Precipitating flux calculated by GEMSIS-RBW
Electron differential flux [/cm²-sr-s-keV]
10⁴
10²
10⁰
10⁻²
10⁻⁴
100
200
300
500
800
Energy [keV]